Article

# g-C$_3$N$_4$/Chlorocobaloxime Nanocomposites as Multifunctional Electrocatalysts for Water Splitting and Energy Storage

Subramanian Sowmya and Vijendran Vijaikanth*

Cite This: *ACS Omega* 2023, 8, 32940−32954

Read Online

ACCESS | Metrics & More | Article Recommendations | Supporting Information

**ABSTRACT:** Due to environmental contamination and the depletion of energy supplies, it is very important to develop low-cost, high-performance, multifunctional electrocatalysts for energy conversion and storage systems. Herein, we report the development of cost-effective modified electrodes containing g-C$_3$N$_4$/chlorocobaloxime composites (C1−C4) and their electrocatalytic behavior toward the hydrogen evolution reaction (HER) and the oxygen evolution reaction (OER), followed by their energy-storage applications. A series of chlorocobaloximes {ClCo(dpgH)$_2$B} with diphenylglyoxime (dpgH) and neutral bases (B) containing a carboxylic acid moiety (isonicotinic acid, pyridine-3,5-dicarboxylic acid, indole-2-carboxylic acid, and p-aminobenzoic acid) have been synthesized and characterized by spectroscopic techniques. The nanocomposites of g-C$_3$N$_4$/chlorocobaloximes are prepared and characterized by Fourier transform infrared (FTIR) spectroscopy, ultraviolet−visible diffuse reflectance spectroscopy (UV-DRS), X-ray diffraction (XRD), scanning electron microscopy (SEM), transmission electron microscopy (TEM), high-resolution TEM (HRTEM), X-ray photoelectron spectroscopy (XPS), particle size distribution analysis (PSA), Brunauer−Emmett−Teller (BET), and energy dispersive X-ray analysis (EDAX) techniques. The composite coatings exhibit enhanced HER performance at lower overpotential and with a lower Tafel slope. When the water-splitting reactions are studied using 0.5 M H$_2$SO$_4$ and 0.5 M KOH as electrolytic solutions, the composite g-C$_3$N$_4$/C2 containing pyridine-3,5-dicarboxylic acid as a neutral base shows excellent HER activity with a lower overpotential of 173 mV at −10 mA cm$^{-2}$ and OER activity with a lower overpotential of 303 mV. The HER reaction takes place through the Volmer−Heyrovský mechanism, where the desorption step is the rate-determining step. Among the synthesized nanocomposites, the nanocomposite g-C$_3$N$_4$/C2 shows higher efficiency toward both HER and OER reactions, with a lower Tafel slope of 55 mV dec$^{-1}$ for HER and 114 mV dec$^{-1}$ for OER than the other nanocomposites. The overall water-splitting studies of the composite g-C$_3$N$_4$/C2 in 0.5 M KOH indicate that the evolution of hydrogen and oxygen occurs constantly up to 120 h. The supercapacitance applications studied using cyclic voltammetry and charge−discharge studies indicate that the nanocomposite g-C$_3$N$_4$/C1 shows a good specific capacitance of 236 F g$^{-1}$ at 0.5 A g$^{-1}$ compared to others. The increased electrochemical performance of the synthesized nanocomposites is due to the incorporation of electron-withdrawing carboxylic-acid-functionalized neutral bases present in cobaloximes, which increases electron mobility. The incorporation of a cobaloxime complex into a g-C$_3$N$_4$ nanosheet enhances the electrocatalytic behavior of the nanosheet, and its performance can further be fine-tuned by systematic variation in the structure of cobaloxime by changing the halide ion, dioxime, the neutral base ligand, or the substituent.
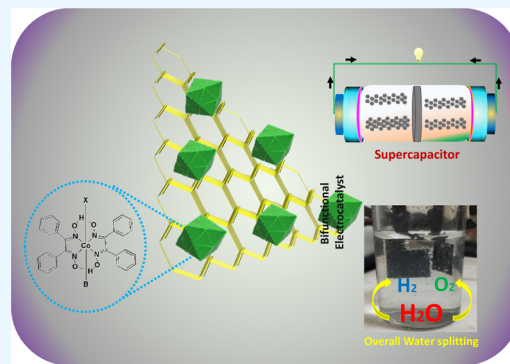
## 1. INTRODUCTION

The issue of energy scarcity and environmental damage caused by the heavy usage of fossil fuels has sparked considerable concern. Therefore, there is a continuous interest in the production of clean, alternative, and sustainable energy sources since nonrenewable energy sources are not constant, and they cannot be used endlessly as power sources.[1−3] Progress in this approach will definitely reduce the release of greenhouse gases and the overdependence on fossil fuels. For developing a stable and efficient renewable energy system, two essential components namely energy conversion and energy-storage capacity are essential.[4,5] Converting renewable energy to chemical energy storage in the form of hydrogen by water splitting is a promising and viable solution to this challenging

problem. In a water-splitting reaction, water can be split into two chemical forms such as hydrogen and oxygen through electrocatalytic reactions, namely, the hydrogen evolution reaction [HER] and the oxygen evolution reaction [OER], respectively.[6−9] But the higher overpotential values of HER and OER limit their electrocatalytic efficiencies as the quantity
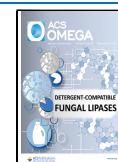
of hydrogen and oxygen adsorbed on the catalyst surface has a substantial impact on the catalyst's activity.[10,11] According to the literature reports, the most advanced electrocatalytically active electrode materials, which have less overpotential, are platinum, iridium oxide, and ruthenium oxide.[12,13] However, due to their cost considerations, they could not be used on a larger scale. It is therefore essential to look for bifunctional platinum-free catalysts that simultaneously catalyze HER and OER reactions.[14] Many earth-abundant transition metal sulfides, nitrides, phosphides, hydroxides/oxides, carbides, and transition metal complexes have been explored as bifunctional catalysts for electrochemical water-splitting applications.[15]

Similarly, developing a storage device with high efficiency and low cost is also a challenge. Most of the storage devices used nowadays are Li-ion batteries and supercapacitors. In Li-ion batteries, when the charge and discharge processes take place, they undergo a deintercalation reaction, but their specific capacity is lost during increasing cycle time or current density. This is the major drawback of using these batteries for future use including portable electronics, medical devices, etc.[16] In terms of power density and energy density, supercapacitors can replace batteries and conventional capacitors.[17] Meanwhile, due to their fast charge–discharge rate and extended lifetime, supercapacitors have attracted significant research attention as efficient energy-storage systems.[18]

Many of the transition-metal-based molecular electrocatalysts can function as the most efficient catalysts in nonaqueous solvents than the aqueous solvents which limit their usage for commercial applications.[19] Additionally, these metal complexes degrade in acidic media, which affects their stability and lowers their water splitting and supercapacitor efficiency. Therefore, at present, research work in this area is focused on developing catalysts with high efficiency and stability in an aqueous medium. For this purpose, a lot of researchers have validated that encapsulation of metal complexes inside a carbon-based substrate, such as graphene, carbon nitrides, etc., increases the stability and efficiency of water splitting and supercapacitor applications and other applications.[20,21] Among the reported carbon substrate materials, two-dimensional carbon nitride ($g$-$C_3N_4$),[22−26] having higher nitrogen content, is gaining importance as a catalyst for supercapacitor and water-splitting applications in recent times.[25,27] However, it possesses fewer active sites and high resistance that limit their applications. To overcome this issue, $g$-$C_3N_4$ combined with metal complexes or metal oxides has been explored and it has been found that the introduction of these catalysts increases its active site, thereby increasing its efficiency.[28,29] Several $g$-$C_3N_4$ composites with metal oxides,[30] metals,[31] carbon,[32] and metal phosphides[33] have been studied for water-splitting activity, and it has been found that the catalyst's incorporation into the $g$-$C_3N_4$ matrix improves the performance.

Carbon, metal oxides, and polymer electrodes have generally been used for supercapacitor applications. Recently, a graphite sheet electrode has been given more importance than the other carbon electrodes for studying the electrocatalytic and supercapacitor applications as the graphite sheet electrode is more cost-effective than CNT,[34] ITO,[35] GCE,[36] etc. Moreover, the graphite sheet electrode has excellent electrical conductivity and high porosity. This property of the graphite sheet electrode can enhance the efficiency in both storage and

energy conversion applications.[37] Nowadays, transition metals have recently been employed extensively in electrode materials for supercapacitor applications as they are affordable, simple to acquire, have more redox valence states, have stable structures, and have outstanding chemical and physical properties. These properties can speed up the charging and discharging process and also allow full contact between the electrode material and the electrolyte.[38,39]

Significant advancement in the area of research on cobaloxime complexes {having general formula $XCo(L)_2B$ (where X = monoanion, L = dioxime monoanion, and B= neutral bases)}, considered as the better model complexes of vitamin $B_{12}$, has taken place over the period of time particularly in the area of catalysis. Their advantages include closer simulation of the reactions of vitamin $B_{12}$-based enzymes, facile synthesis, and more importantly, fine-tuning of the electronic and steric properties of the axial (X, B) and equatorial (L) ligands can be done effortlessly. Recently, a lot of importance has been devoted to the application of cobaloxime complexes toward photocatalytic and electrocatalytic hydrogen evolution reactions.[40] The electrocatalytic activity of the cobaloxime complexes with $MoS_2$,[41] graphene,[42] and MOF[43] has been reported earlier. The $g$-$C_3N_4$/cobaloxime nanocomposites have been studied extensively for their photocatalytic activity,[30,44] but the electrocatalytic activity of $g$-$C_3N_4$ and $g$-$C_3N_4$/cobaloxime composites has not been explored much. Similarly, the supercapacitor application of cobaloxime complexes has not yet been reported yet. Among the reported cobaloximes, most of the cobaloximes are known with dimethyl glyoximes (dmgH) as an equatorial ligand, and complexes with other dioximes are relatively unexplored. Also, the electrocatalytic properties of cobaloximes containing diphenyl glyoximes have not been probed yet, and in particular, the electrocatalytic activity of modified electrodes containing cobaloximes with diphenylglyoxime and functionalized neutral bases has not been studied. It is well established that the effect of the substituent plays a vital role in the reactivity of cobaloxime complexes.

Keeping all of the above facts, we report here the synthesis, characterization, and electrocatalytic applications of cost-effective $g$-$C_3N_4$/chlorocobaloxime nanocomposites containing carboxylic acid functionality. For this study, a series of chlorocobaloxime complexes with diphenyl glyoximes and neutral bases containing carboxylic acid functionality have been synthesized and characterized. The synthesized complexes have been converted into nanocomposites with $g$-$C_3N_4$, and the characterization of the synthesized nanocomposites using various techniques is described. Finally, the composites have been coated on the graphite sheet electrode, and their utilization toward overall water-splitting (HER and OER) reactions and supercapacitor applications are discussed.

## 2. EXPERIMENTAL SECTION

**2.1. Chemicals and Reagents.** Urea powder ($CH_4N_2O$)-97% (Himedia), cobalt chloride hexahydrate ($CoCl_2\cdot6H_2O$)-97% (Avra), isonicotinic acid ($C_6H_5NO_2$)-99% (Sigma-Aldrich), $p$-aminobenzoic acid ($C_7H_7NO_2$)-99% (Alfa Aeser), indole-2-carboxylic acid ($C_9H_7NO_2$)-95% (Avra), pyridine-3,5-dicarboxylic acid ($C_7H_5NO_4$)-97% (Avra), acetonitrile ($CH_3CN$) (Avra), and ethanol ($C_2H_5OH$)—analytical grade were purchased and used without further purification. The graphite sheet electrode with a 0.5 mm thickness was used as a working electrode.

**Scheme 1. General Scheme for the Synthesis of Chlorocobaloximes**
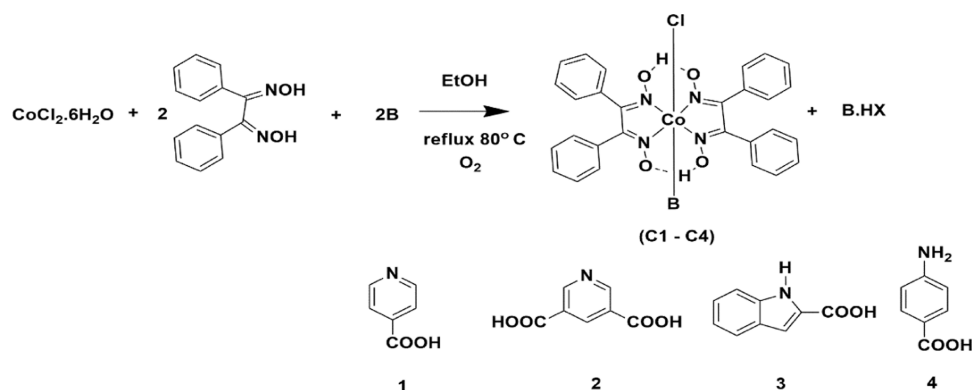


## 2.2. General Procedure for the Synthesis of Chlorocobaloximes.
Chlorocobaloximes were synthesized by the general procedure as given below (Scheme 1). To a refluxing solution of $CoCl_2 \cdot 6H_2O$ (4.2 mmol) and $dpgH_2$ (8.4 mmol) in 40 mL of ethanol, the base [isonicotinic acid (1), pyridine-3,5-dicarboxylic acid (2), indole-2-carboxylic acid (3) and p-aminobenzoic acid (4)] (8.4 mmol) was added with constant stirring. The mixture was refluxed for 6 h and allowed to cool to room temperature. Air was passed through the solution for 2 h. The brown microcrystalline precipitate formed was filtered off, washed with a solvent [2 × 10 mL], and dried under a vacuum to get the desired product, and the complexes were characterized by spectroscopic techniques.[45,46]

## 2.3. Synthesis of g-C₃N₄.
The polymeric $g\text{-}C_3N_4$ was synthesized by a simple pyrolysis method reported by Dong et al.[47] Ten grams of urea powder was taken in an alumina crucible, covered tightly, and heated up to 450 °C in a muffle furnace for 2 h. After cooling, the yellow flake powder obtained was collected, washed with distilled water, and used for further synthesis.

## 2.4. Synthesis of g-C₃N₄/Chlorocobaloxime Nanocomposites.
The $g\text{-}C_3N_4$/chlorocobaloxime nanocomposites were prepared as follows: 250 mg of $g\text{-}C_3N_4$ was dispersed ultrasonically in 10 mL of an acetonitrile solution followed by the addition of 125 mg of chlorocobaloximes. The mixture was ultrasonicated for 2 h and refluxed overnight at 95 °C under a nitrogen atmosphere. The resulting solution was washed several times in ethanol and distilled water by centrifugation to remove unbound cobaloximes.[48] The formed $g\text{-}C_3N_4$/chlorocobaloxime nanocomposites (Table 1) were used for catalysis after drying.

## 2.5. Instrumentation.
IR spectra were recorded using KBr Pellets on a Shimadzu FTIR Spectrometer. Ultraviolet−visible diffuse reflectance spectroscopy (UV-DRS) spectra were recorded on a Jasco v-630 spectrometer using quartz glass. X-ray diffraction was recorded using an X-Shimadzu instru-

ment. Scanning electron microscopy (SEM) analysis was carried out on a JEOL, JSE-6390 SEM. The transmission electron microscopy (TEM) image was recorded using a JEM 2100 instrument. High-resolution transmission electron microscopy (HRTEM) equipped with a Gatan USC 4000 4 × 4k camera at an accelerating voltage of 200 kV was used. Brunauer−Emmett−Teller (BET) was analyzed using the Nova station A instrument. Particle size analysis was carried out on a zeta sizer nano ZS₉₀. EDAX spectra were recorded on a JSE-6390. X-ray photoelectron spectroscopy (XPS) was recorded using a Thermo Scientific Nexa spectrometer, UHV.

## 2.6. Electrochemical Investigation.
The electrochemical studies were carried out on PAR electrochemical workstation PMC CHS08A using a graphite sheet working electrode [1 × 1 cm²], Ag/AgCl (3 M KCl) as a reference electrode, and a platinum wire as a counter electrode without $iR$ compensation. A 0.5 M $H_2SO_4$ solution was used as an electrolyte solution for HER and supercapacitor studies. OER was carried out using a 0.5 M KOH solution as an electrolyte. The observed potentials were converted to reversible hydrogen electrode potential (RHE) by using the equation $E_{RHE} = E_{Ag/AgCl} + 0.209$ V + 0.059 V × pH. For calculating overpotentials in the OER, the relationship $E_{RHE} - 1.23$ V was used.

## 2.7. Fabrication of the Electrode for HER, OER, and Overall Water Splitting.
A graphite sheet electrode of 1 × 1 cm² with a 0.5 mm thickness was used as a working electrode for HER, OER, and overall water splitting. The prepared composites were coated by the drop-casting method by the following procedure. The synthesized nanocomposites and N-methyl-2-pyrrolidone (NMP) were taken in a 9:1 ratio and added to a Nafion solution (aqueous dispersion) and then sonicated for 2 h to make a slurry. The slurry was evenly coated over the graphite sheet electrode. The electrode was weighed after being dried overnight. The catalyst loading on the electrode was found to be 1 mg.

## 2.8. Fabrication of Electrodes for Supercapacitor Applications.
A graphite sheet electrode of 1 × 1 cm² with a 0.5 mm thickness was used as a working electrode, and the prepared composites were coated by the drop-casting method by the following procedure. The synthesized nanocomposites, poly(vinylidene fluoride) (PVDF-binder), and carbon black were taken in an 8:1:1 ratio and added to N-methyl-2-pyrrolidone (NMP) and then sonicated for 2 h to make a slurry. The slurry was evenly coated over the graphite sheet electrode. The electrode was weighed after overnight drying. The catalyst loading on the electrode was found to be 1 mg.

**Table 1. Synthesized g-C₃N₄/Chlorocobaloximes**

| S. No | nanosheet | complex | composite name |
|---|---|---|---|
| 1 | g-C₃N₄ | ClCo(dpgH)₂(Isonicotinic acid) (C1) | g-C₃N₄/C1 |
| 2 | g-C₃N₄ | ClCo(dpgH)₂(Pyridine-3,5-dicarboxylic acid) (C2) | g-C₃N₄/C2 |
| 3 | g-C₃N₄ | ClCo(dpgH)₂(Indole-2-carboxylic acid) (C3) | g-C₃N₄/C3 |
| 4 | g-C₃N₄ | ClCo(dpgH)₂(p-Aminobenzoic acid) (C4) | g-C₃N₄/C4 |

## 3. RESULTS AND DISCUSSION

**3.1. IR Spectroscopy.** IR spectroscopy has been used to confirm the functional groups present in cobaloxime complexes and pure g-$C_3N_4$ and g-$C_3N_4$/cobaloxime nanocomposites. Figure 1 depicts the IR spectrum of cobaloxime
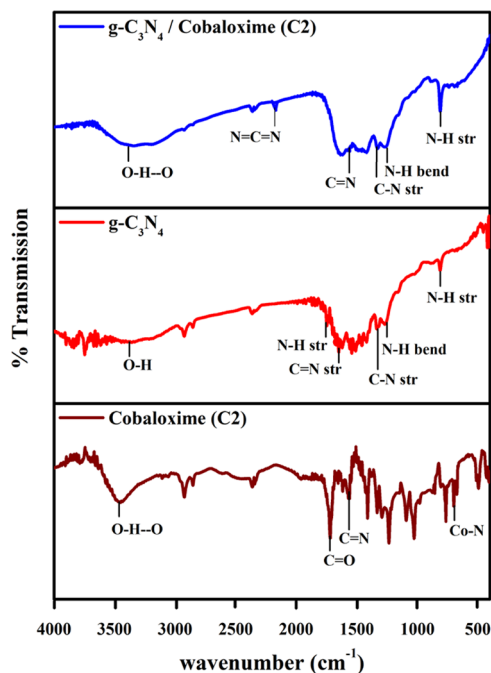


**Figure 1.** IR spectrum of cobaloxime (C2), g-$C_3N_4$, and g-$C_3N_4$/cobaloxime (C2).

(C2), g-$C_3N_4$, and g-$C_3N_4$/C2. In the IR spectra of pure g-$C_3N_4$, the characteristic peak at around 3360 cm$^{-1}$ is attributed to O−H stretching, the peak at 1743 cm$^{-1}$ is due to N−H stretching, 1639 cm$^{-1}$ is assigned to C≡N stretching, the peaks at 1521 and 1240 cm$^{-1}$ are due to stretching and bending frequency of N−H, the peak at 1328 cm$^{-1}$ is due to aromatic C−N stretching, and a peak at 812 cm$^{-1}$ is due to the bending mode of N−H stretching.[49]

All of the synthesized chlorocobaloxime complexes show a characteristic peak at around 600−700 cm$^{-1}$, corresponding to Co−N stretching. The C≡N stretching of the complexes appears at around 1500−1600 cm$^{-1}$. The presence of the C≡O group is confirmed by the appearance of a peak at around 1700 cm$^{-1}$ for all of the complexes. The 3400−3500 cm$^{-1}$ peak is due to O−H···O stretching.[50]

In the nanocomposite, all of the characteristic peaks present in both pure g-$C_3N_4$ and chlorocobaloximes appeared, but there was a slight shift in the position of the peaks. These shifts in the characteristic peaks indicate the formation of nanocomposites. Also, the new peak that appears at around 2150 cm$^{-1}$ is observed only in the composite, which is due to N≡C≡N that indicates the accumulation of electrons on g-$C_3N_4$ layers, pointing to a Coulombic mechanism of intercalation.[51]

**3.2. UV-DRS Spectroscopy.** The UV-DRS spectra of the g-$C_3N_4$ and g-$C_3N_4$/cobaloxime (C1−C4) nanocomposites are depicted in Figure 2.

The UV-DRS spectra show that pure g-$C_3N_4$ absorbs at around 390 nm, whereas the composites absorb at around 370 nm. In addition to the 370 nm peak, a broad peak has been observed at around 280 nm. The shift in the absorbance and
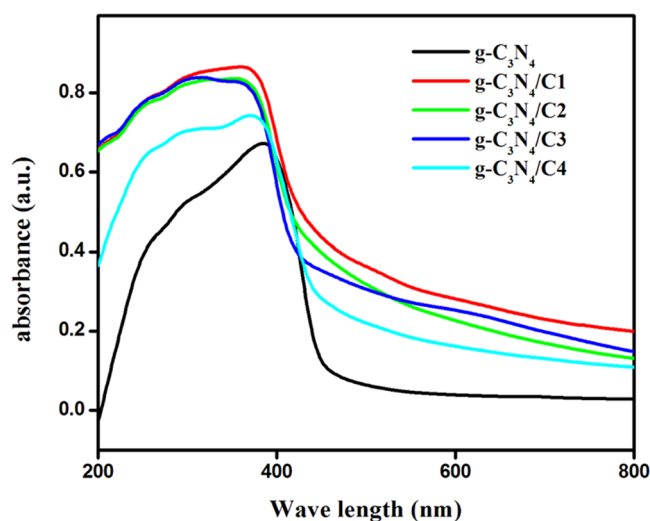


**Figure 2.** UV-DRS spectra of g-$C_3N_4$, g-$C_3N_4$/cobaloxime nanocomposites (C1−C4).

the appearance of additional peaks in the composite material indicate the formation of nanocomposites of g-$C_3N_4$/cobaloxime. The Tauc plot (Figure S1) has been used to calculate the band gap of g-$C_3N_4$ and g-$C_3N_4$/ nanocomposites (Table S1).

**3.3. X-ray Photon Spectroscopy.** To gain insights into the binding energy, electronic states, and chemical composition of the composite, the g-$C_3N_4$/C2 composite has been characterized by X-ray photoelectron spectroscopy. Figure 3a shows the survey spectrum of the g-$C_3N_4$/C2 composite, which confirms the presence of the elements C, O, N, Cl, and Co. The wide range spectrum contains five predominant peaks at 285, 533, 400, 200, and 782 eV, confirming the presence of chemical functional groups of C, O, N, Cl, and Co, respectively. The high-resolution deconvoluted spectrum of C 1s shows peaks at 285.1 285.8, and 289.2 eV, corresponding to C−C, C≡N, and C−(N)$_3$, respectively (Figure 3b). Figure 3c shows that the O 1s spectra deconvoluted into two main peaks. The primary peak corresponds to C−O−C at 533.7 eV and the secondary peak represents the carbon double bond with oxygen (C≡O) at 532.2 eV. As shown in Figure 3d, the N 1s spectrum is deconvoluted into four intense peaks. The intense peak centered at 398.6 eV confirms the presence of deprotonated N atoms corresponding to C−N−C bonds in the g-$C_3N_4$ moiety. Similarly, the other three peaks with binding energies of 399.3, 400.5, and 402 eV represent the C≡NH, C≡N bonds, and tertiary sp3 nitrogen atoms (N−C3) respectively. The high-resolution Cl 2p XPS spectrum (Figure 3e) exhibits doublets at 198.5 and 200.2 eV associated with 2p$_{3/2}$ and 2p$_{1/2}$ levels due to the Co−Cl covalent bond in the cobaloxime complex, respectively. In Figure 3f, the Co 2p spectrum exhibiting the peaks at 781.5 and 796 eV is attributed to the valence states of Co 2p$_{3/2}$ and Co 2p$_{1/2}$ respectively

**3.4. X-ray Diffraction (XRD).** The phase and the crystallite nature have been studied by using X-ray diffraction analysis. The XRD patterns of pure g-$C_3N_4$ and g-$C_3N_4$/C2 nanocomposites are provided in Figure 4. The pure g-$C_3N_4$ shows a peak at 27.58° with an interlayer distance of 0.32 nm and a shoulder peak at 13.7° with an interlayer distance of 0.57 nm, and the peaks have been assigned to the (002) and (100) planes, respectively, according to JCPDS indexing (36-1472). For g-$C_3N_4$/cobaloxime composites, the peak at 27.58° is

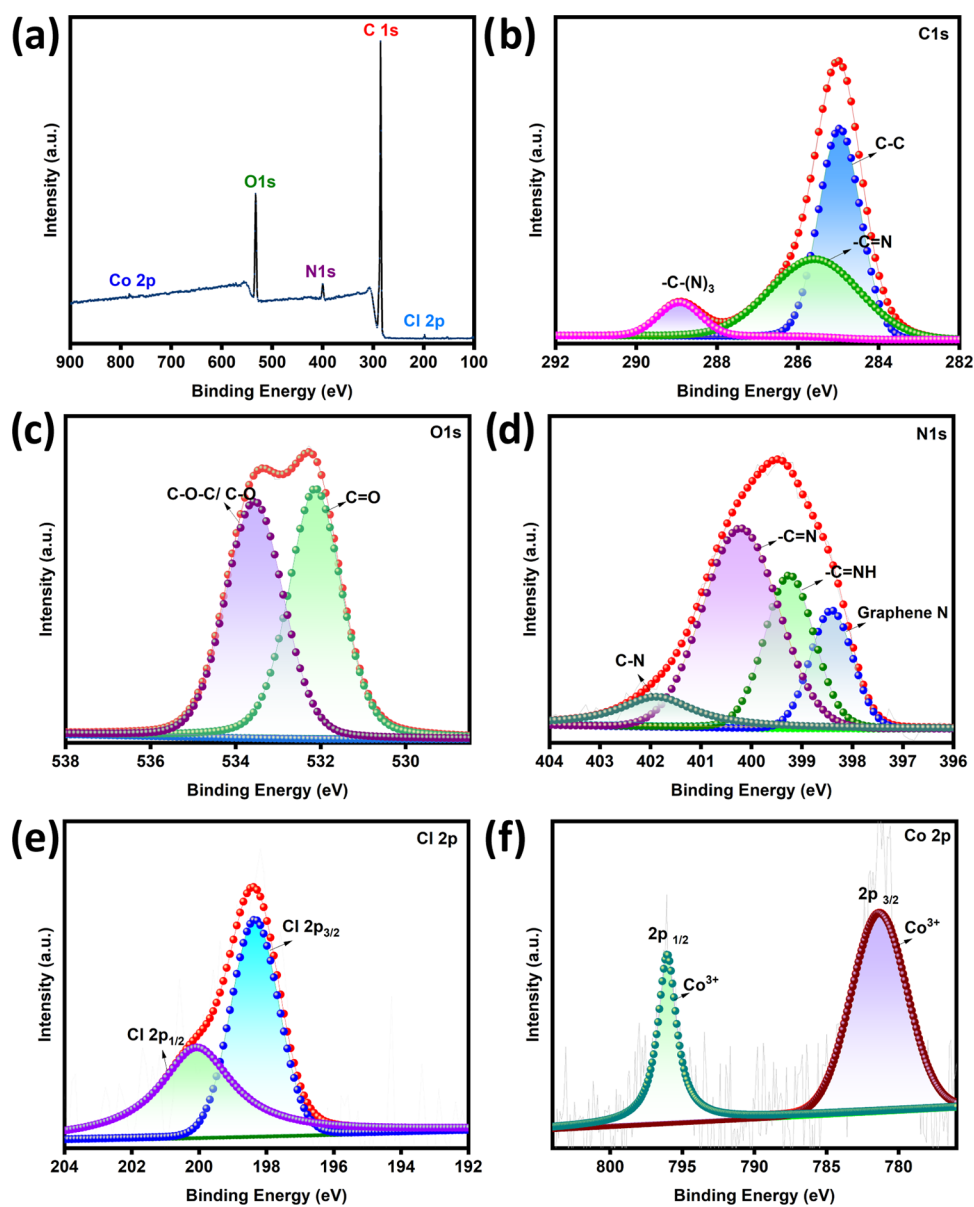**Figure 3.** (a) Full XPS spectrum of g-C₃N₄/C2 and high-resolution XPS spectra of (b) C 1s, (c) O 1s, (d) N 1s, (e) Cl 2p, and (f) Co 2p.

slightly shifted toward a lower $2\theta$ value (Figure S2) and also there is a slight increase in the *d*-spacing, which may be to the interaction between the $NH_2$ moiety of $C_3N_4$ and the COOH moiety of the cobaloxime complex that makes the intercalation of cobaloxime into the g-$C_3N_4$ nanosheet.[26,52,53] The grain sizes of g-$C_3N_4$ and g-$C_3N_4$/cobaloxime composites have been calculated using the Scherrer equation, and values are given in Table 2. The absence of any other impurity peak in the diffraction pattern shows the higher purity of the nano-composites.

**3.5. Brunauer−Emmett−Teller (BET) Analysis.** The pore structure and the specific surface area of the synthesized g-$C_3N_4$ and g-$C_3N_4$/C2 samples have been analyzed by $N_2$ adsorption−desorption isotherms and Barrett−Joyner−Halenda (BJH) pore size distribution (Figure 5). The adsorption−desorption isotherms of g-$C_3N_4$ and g-$C_3N_4$/C2 exhibit type IV isotherm with H3 hysteresis loops, which indicates that both the samples have a mesoporous structure.[54] The hysteresis loop indicates the formation of nonrigid aggregates

of flake-like particles. The surface area of g-$C_3N_4$/C2 material was calculated as 80.341 $m^2$ $g^{-1}$, which is higher than the g-$C_3N_4$ nanosheet (76.487 $m^2$ $g^{-1}$). Moreover, the hysteresis loop of g-$C_3N_4$/C2 is shifted to the lower relative pressure, and the area of the hysteresis loop was larger than that of g-$C_3N_4$, indicating that g-$C_3N_4$/C2 has an enlarged mesoporous structure. The intercalation of cobaloxime between the interlayers of g-$C_3N_4$ induces the building of mesoporous structures, which results in an increase in the number of electroactive sites and hybrid material utilization. The pore distribution plot of g-$C_3N_4$ and g-$C_3N_4$/C2 is depicted in Figure 5 (inset). The significant enlargement of the nanopores was observed in g-$C_3N_4$/C2 with a larger pore volume of 0.169 $cm^3$ $g^{-1}$ compared with the g-$C_3N_4$ nanosheet (0.157 $cm^3$ $g^{-1}$). The higher pore size distribution of g-$C_3N_4$/C2 is due to the presence of abundant active sites and it increases the transfer resistance of the electrolyte and the catalyst.[55]

**3.6. Scanning Electron Microscopy (SEM) Analysis.** Scanning electron microscopy (SEM) analysis has been carried
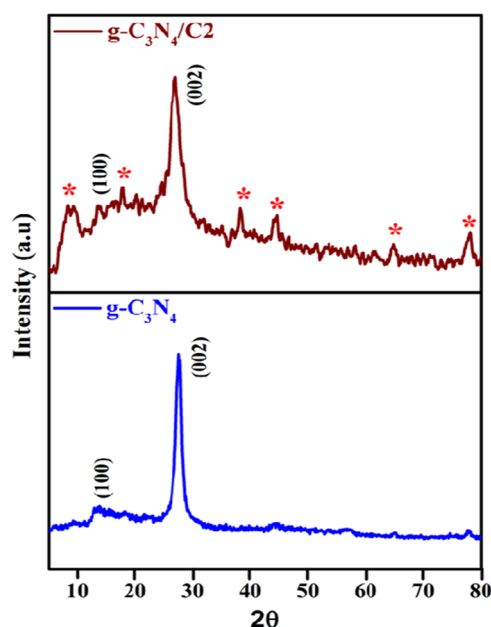
**Figure 4.** XRD pattern of g-C$_3$N$_4$ and g-C$_3$N$_4$/C2 (*—due to the cobaloxime complex (Figure S2)).

**Table 2. XRD Data of g-C$_3$N$_4$ and g-C$_3$N$_4$/Cobaloxime Nanocomposites**

| compound | peaks | grain size in Å | d-spacing in nm |
|---|---|---|---|
| g-C$_3$N$_4$ | 27.60 | 6.40 | 0.323 |
| g-C$_3$N$_4$/C1 | 27.30 | 2.85 | 0.327 |
| g-C$_3$N$_4$/C2 | 26.95 | 3.29 | 0.331 |
| g-C$_3$N$_4$/C3 | 27.14 | 3.34 | 0.329 |
| g-C$_3$N$_4$/C4 | 27.38 | 6.06 | 0.326 |
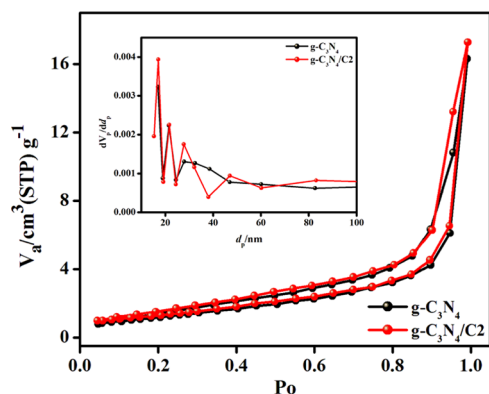


**Figure 5.** BET analysis of g-C$_3$N$_4$ and g-C$_3$N$_4$/C2 composites (inset: the pore distribution curve of g-C$_3$N$_4$ and g-C$_3$N$_4$/C2).

out to understand the morphology of the prepared nanocomposites. The SEM images of g-C$_3$N$_4$, cobaloxime complex **C2**, and g-C$_3$N$_4$/C2 are given in Figure 6. The pure g-C$_3$N$_4$, cobaloxime **C2**, and g-C$_3$N$_4$/C2 nanocomposites show flake-like, cube-like, and deformed flake-like morphologies, respectively. The deformation of the flakes is due to the intramolecular interaction between g-C$_3$N$_4$ and cobaloxime complex **C2**.

**3.7. Energy Dispersive X-ray Analysis (EDAX).** The EDAX spectrum has been recorded for pure g-C$_3$N$_4$, cobaloxime complex (**C2**), and g-C$_3$N$_4$/ C2 nanocomposites to confirm the presence and approximate weight % of the

elements in it (Figures 7 and S3). The approximate weight % details are given in Table S2. The spectrum shows that pure g-C$_3$N$_4$ contains only carbon, nitrogen, and oxygen. Cobaloxime contains cobalt and chlorine elements in addition to carbon, nitrogen, and oxygen. The nanocomposite contains all of the elements present in g-C$_3$N$_4$ and the cobaloxime complex. This shows the formation of a nanocomposite, and no other impurities are present in the nanocomposite.

**3.8. Transmission Electron Microscopy (TEM) Analysis.** The TEM has been recorded to analyze the morphology of g-C$_3$N$_4$, cobaloxime **C2**, and g-C$_3$N$_4$/C2 nanocomposites. The TEM images are given in Figure 8. From the figure, it can be observed that g-C$_3$N$_4$ tends to have a two-dimensional sheet-like morphology. Cobaloxime **C2** shows a crystal-like morphology. The cobaloxime complexes can be seen on the g-C$_3$N$_4$ surface in black color, which affirms that the cobaloxime complexes are embedded in the g-C$_3$N$_4$ matrix. g-C$_3$N$_4$/C2 nanosheets exhibit a stacked lamellar structure with an irregular flake-like two-dimensional morphology.

In addition to TEM images, the HRTEM of the g-C$_3$N$_4$/C2 nanocomposite has been recorded to analyze the width and thickness of the composite (Figure 9). Recorded at different resolutions, the images in Figure 9a,b indicate a lamellar 2D structure similar to the TEM images of the g-C$_3$N$_4$/C2 nanocomposite. The interplanar distance has been found to be 0.33 nm from the SAED pattern (Figure 9b, inset), which matches well with the crystal lattice of the (002) plane, and the result is concurrent with the XRD analysis.

**3.9. Particle Size Distribution Analysis (PSA).** To study the particle size of the compounds, particle size analysis was carried out using an aqueous dispersion of the samples. The corresponding bar graphs are given in Figure 10. The pure g-C$_3$N$_4$ has a particle size of 690 nm with a 124.5 nm width. Cobaloxime complex **C2** has a particle size of 318.5 nm with an 88.33 nm width. The g-C$_3$N$_4$/C2 composite shows a particle size of 141.2 nm with a 22.42 nm width. The decrease in the particle size is due to the intercalation of the metal complex into the g-C$_3$N$_4$ nanosheet. The decrease in particle size in the composite indicates that the catalytic activity of the complex is enhanced.[56]

**3.10. Hydrogen Evolution Reaction Performance.** The synthesized cobaloxime complexes have been employed as electrocatalysts after intercalation with g-C$_3$N$_4$ nanosheets to improve the HER activity since some cobalt complexes have been reported to show good HER activity. The linear scan voltammetry technique was employed to study the HER activity of the synthesized composites (Figure 11a). For this purpose, the HER activity was studied in a 0.5 M KOH solution initially but the composite materials showed higher overpotential values in an alkaline medium.[57] Then, the HER studies were performed using the modified graphite sheet electrodes drop-casted with (i) g-C$_3$N$_4$, (ii) cobaloxime **C2**, and (iii) g-C$_3$N$_4$/cobaloxime composites in a 0.5 M H$_2$SO$_4$ solution. The pure graphite sheet shows negligible HER activity. But when the graphite sheet was coated with g-C$_3$N$_4$, the sheet became electroactive and its HER performance was improved, showing an overpotential of 586 mV at a current density of −10 mA cm$^{-2}$ vs RHE. The HER studies performed for the cobaloxime **C2** show an overpotential of 525 mV at −10 mA cm$^{-2}$ vs RHE, which is slightly lower than the g-C$_3$N$_4$ nanosheet. Then, HER studies were conducted on all four synthesized g-C$_3$N$_4$/cobaloxime composites. The overpotential values obtained for g-C$_3$N$_4$/C1, g-C$_3$N$_4$/C2, g-C$_3$N$_4$/C3, and
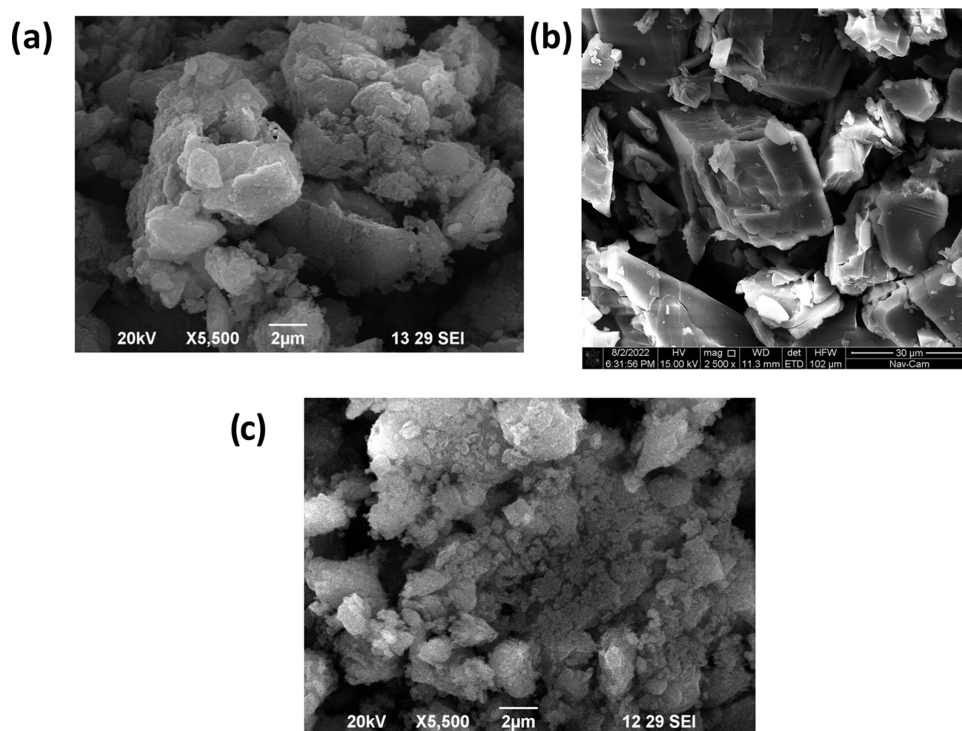
**Figure 6.** Scanning electron microscopy images of (a) g-$C_3N_4$, (b) cobaloxime complex C2, and (c) g-$C_3N_4$/C2.
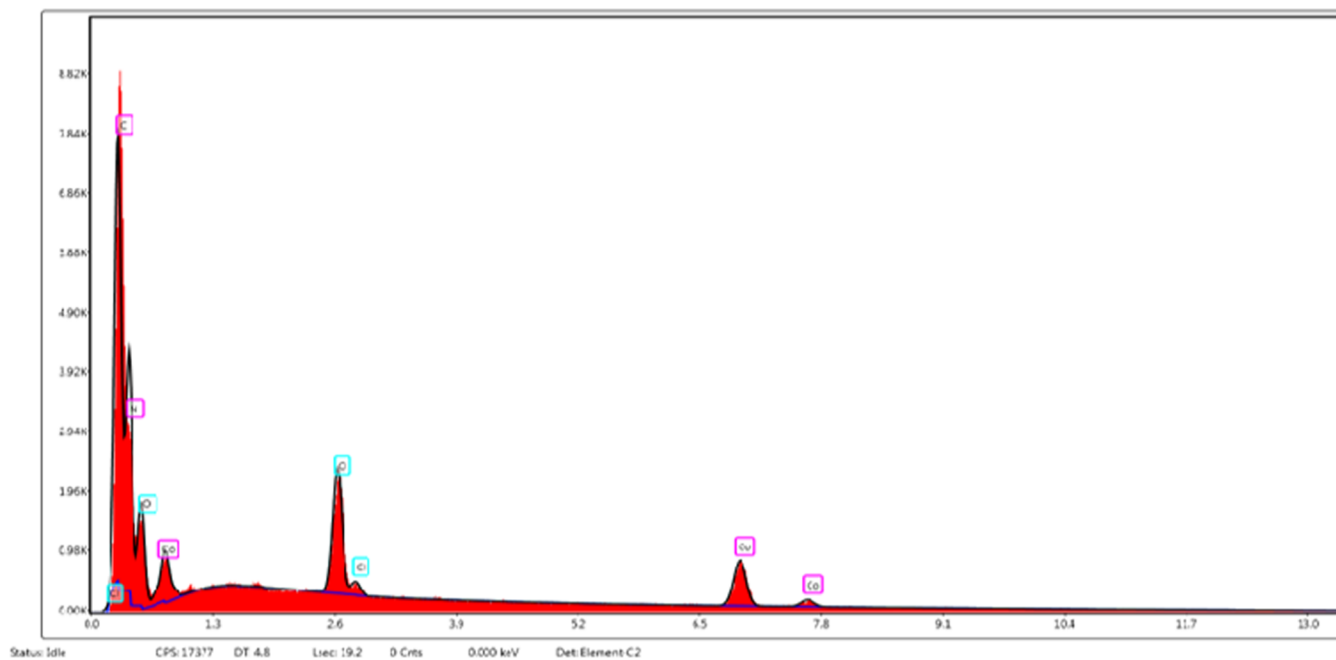


**Figure 7.** EDAX spectra of g-$C_3N_4$/C2.

g-$C_3N_4$/C4 nanocomposites are 199, 173, 264, and 324 mV vs RHE, respectively. The overpotentials of all g-$C_3N_4$/cobaloxime composites were found to be much lower than both the g-$C_3N_4$ and cobaloxime, indicating that the electroactivity of the g-$C_3N_4$nanosheet has been enhanced by the addition of a cobaloxime catalyst. Among the g-$C_3N_4$/cobaloxime composites reported here, the composite g-$C_3N_4$/C2 shows higher activity than those of other nanocomposites.

To study the nature of the electrocatalyst and overall HER activity, the Tafel slope was derived from LSV (Figure 11b).

The g-$C_3N_4$ exhibits a Tafel slope of 312 mV dec$^{-1}$, and cobaloxime complex **C2** exhibits a Tafel slope of 256 mV dec$^{-1}$. The nanocomposites of g-$C_3N_4$/cobaloxime composites exhibit the Tafel slopes of 60, 55, 73, and 76 mV dec$^{-1}$ vs RHE for g-$C_3N_4$/C1, g-$C_3N_4$/C2, g-$C_3N_4$/C3, and g-$C_3N_4$/C4 nanocomposites, respectively. This clearly shows that g-$C_3N_4$/cobaloxime nanocomposites behave as better catalysts than g-$C_3N_4$ and cobaloximes. It also shows that in g-$C_3N_4$/cobaloxime composites, the reaction takes place through the Volmer−Heyrovský mechanism (Scheme 2), where the

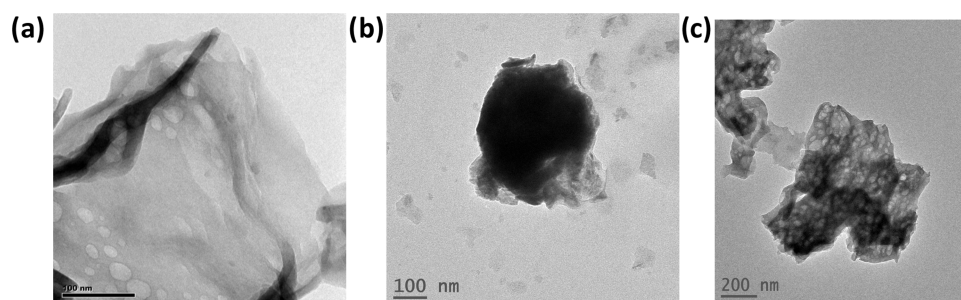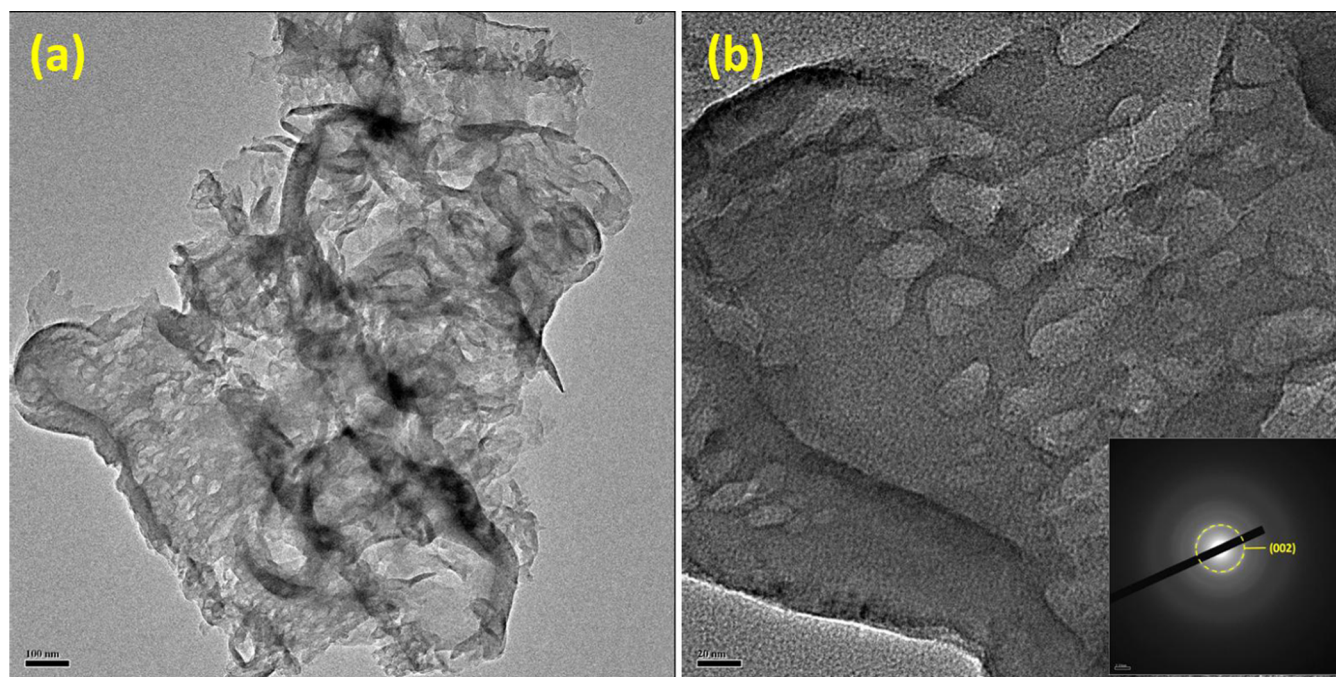**Figure 8.** Transmission electron microscopy images of (a) g-C$_3$N$_4$, (b) cobaloxime complex C2, and (c) g-C$_3$N$_4$/C2.



**Figure 9.** HR-transmission electron microscopy images of g-C$_3$N$_4$/C2 (a) at 100 nm and (b) at 20 nm (inset: SAED pattern).

desorption step is the rate-determining step.[58] Materials with a lower Tafel slope and the highest current density have been proven to be better catalysts and possess good kinetic properties for water reduction applications. Among the four nanocomposites, synthesized g-C$_3$N$_4$/C2 shows a better catalytic activity with a lower Tafel slope and lower onset potential compared to the other three composites synthesized.

Chronoamperometric experiments have been carried out to analyze the stability of the g-C$_3$N$_4$/C2 catalyst, and the chronoamperometric graph is given in Figure 12a. The chronoamperometric studies show that the catalyst is stable up to 15 h at a fixed potential of 173 mV, and LSV was recorded after the chronoamperometric experiments (Figure 12b). The LSV curve shows that there is an increase of only 0.10 mV at a current density of −10 mA cm$^{-2}$. This shows the good stability of the composite.

**3.11. Oxygen Evolution Reaction Performance.** In addition to HER performance, the OER performance has been studied in an alkaline medium to verify the efficient water-splitting ability of the synthesized materials. The LSV graph shows that overpotentials of 498 mV and 404 mV vs RHE are required to drive a 10 mA cm$^{-2}$ current density for the g-C$_3$N$_4$ nanosheet and the cobaloxime complex (C2), respectively (Figure 13a). However, the g-C$_3$N$_4$/cobaloxime composites

need less overpotential to drive 10 mA cm$^{-2}$ than both g-C$_3$N$_4$ and cobaloxime complex C2. The composites show the overpotential values of 322, 303, 376, and 354 mV vs RHE for g-C$_3$N$_4$/C1, g-C$_3$N$_4$/C2, g-C$_3$N$_4$/C3, and g-C$_3$N$_4$/C4 nanocomposites, respectively.

g-C$_3$N$_4$ exhibits a Tafel slope of 296 mV dec$^{-1}$ and cobaloxime complex C2 exhibits a Tafel slope of 253 mV dec$^{-1}$. The g-C$_3$N$_4$/cobaloxime composites g-C$_3$N$_4$/C1, g-C$_3$N$_4$/C2 g-C$_3$N$_4$/C3, and g-C$_3$N$_4$/C4 show the Tafel slope values of 148, 114, 176, and 194 mV dec$^{-1}$, respectively. Similar to HER, the composite g-C$_3$N$_4$/C2 shows good catalytic activity with a lower Tafel slope of 114 mV dec$^{-1}$ (Figure 13b). The plausible mechanism is given in Scheme 3.[15] The intercalation of the cobaloxime complex on g-C$_3$N$_4$ enables high mass transfer within the electrodes.

The catalyst's stability was analyzed by chronoamperometry, and the catalyst was found stable up to 15 h (Figure 14a). The LSV was recorded after the stability experiments, and there was a change of only 0.1 mV, which shows the good stability of the catalyst (Figure 14b). After the chronoamperometric analysis, the SEM image of the catalyst was recorded to check the morphology, and the image showed similar deformed flake-like morphology, and there was no detectable change in the
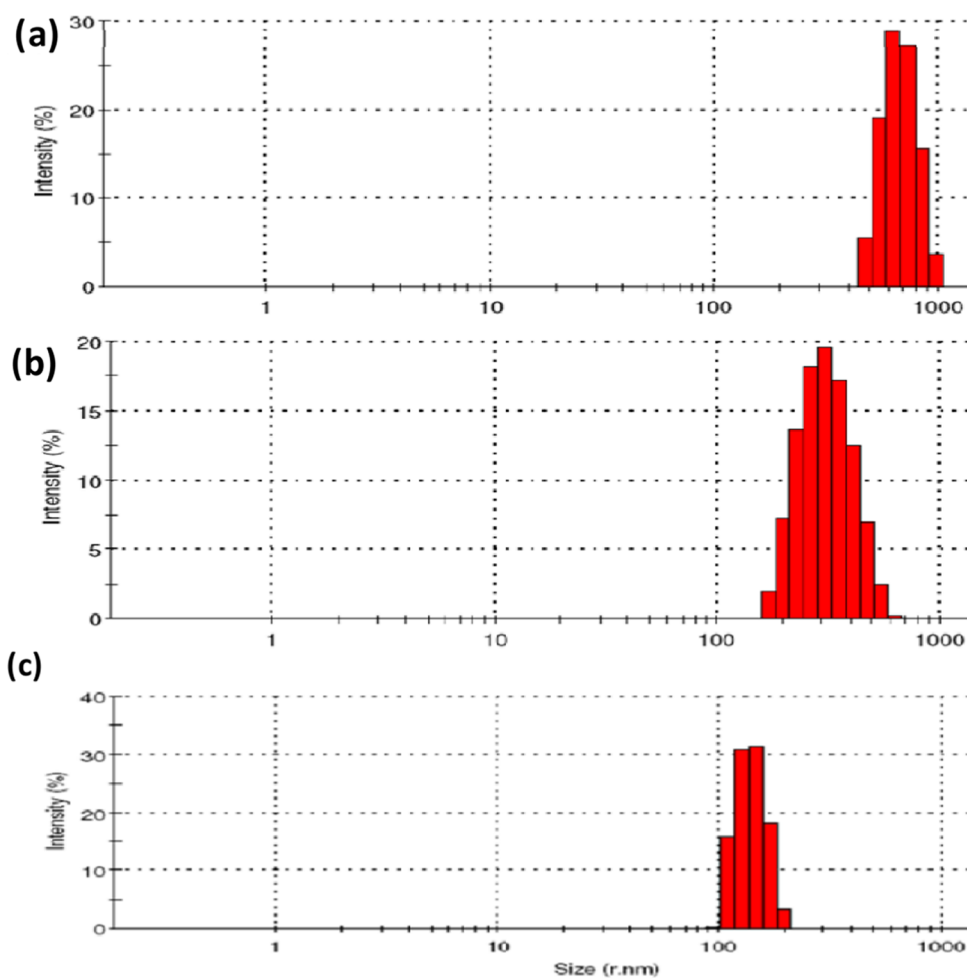
**Figure 10.** Particle size distribution of (a) g-$C_3N_4$, (b) cobaloxime complex C2, and (c) g-$C_3N_4$/C2 composite.
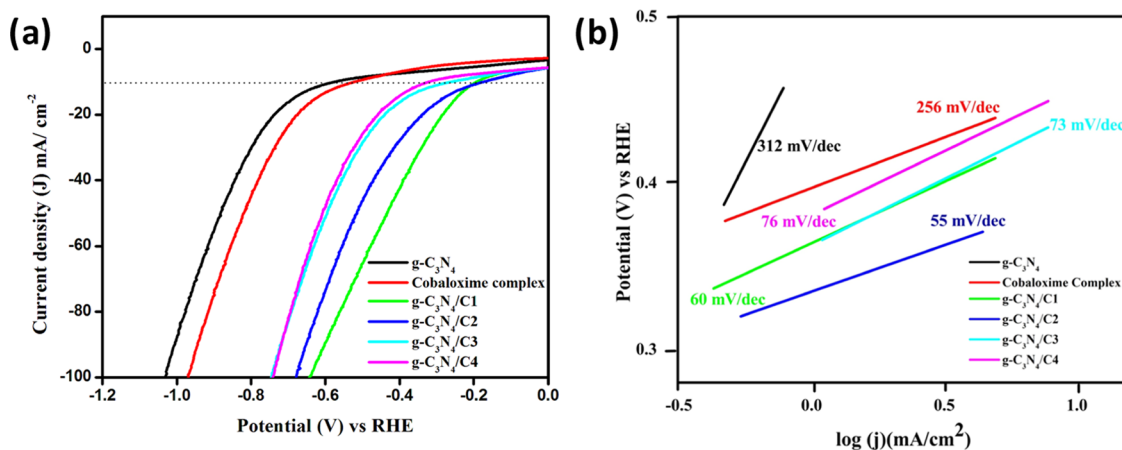


**Figure 11.** (a) Linear sweep voltammograms of g-$C_3N_4$, cobaloxime complex C2, and g-$C_3N_4$/cobaloxime nanocomposites. (b) Tafel slope of g-$C_3N_4$, cobaloxime complex C2, and g-$C_3N_4$/cobaloxime nanocomposites for HER in 0.5 M $H_2SO_4$.

morphology. The SEM image after the stability test is given in Figure S4.

The HER and the OER activities of g-$C_3N_4$/C2 nanocomposites are higher compared to the other nanocomposites synthesized at 10 mA cm$^{-2}$. At higher current density, g-$C_3N_4$/C1 also shows higher activity, but the Tafel slope was lower for the g-$C_3N_4$/C2 composite than for g-$C_3N_4$/C1. It has been reported that the increase in the number of oxygen groups in a composite increases the active sites on the composites, thereby enhancing the water-splitting ability.[59] In the present study, the higher activity of g-$C_3N_4$/C2 nanocomposites may be due to the presence of two carboxylic acid groups, where there is an increased number of oxygen atoms. The comparison Tafel slope values of other earlier g-$C_3N_4$ nanocomposites are given in Table S3.[28,47,60−62] The values were found to be congruent with the earlier reported values.

**Scheme 2. Plausible Mechanism for the HER Reaction (Volmer−Heyrovský)**
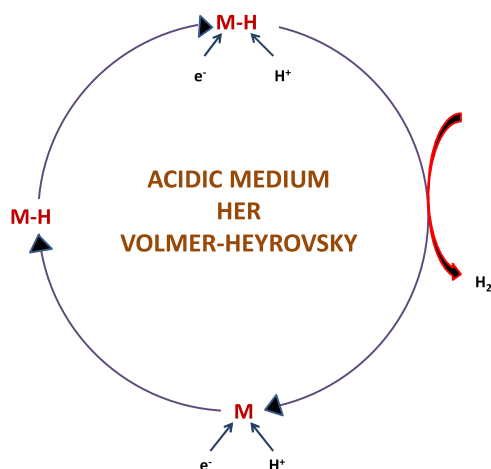


### 3.12. Overall Water Splitting.
After studying the HER and OER activity of the catalysts, the overall water-splitting performance of the catalyst g-C$_3$N$_4$/C2 was carried out in a 0.5 M KOH solution using the graphite sheet electrodes as an anode and a cathode, both coated with 1 mg of the catalyst in a two-electrode system configuration. The LSV curve was recorded, and the overpotential was found to be 1.64 V vs RHE at 10 mA cm$^{-2}$ (Figure 15a). The chronopotentiometric experiment was carried out at 10 mA cm$^{-2}$, and it was found that the overpotential was maintained without disturbance for at least 120 h (Figure 15b). The inset in Figure 15b shows the H$_2$ and O$_2$ bubbles at the electrode surface, indicating an effective electron transfer on both the anode and cathode.

### 3.13. Supercapacitance Applications.
The improved high-rate charge−discharge analysis is an important aspect in determining the energy-storage performance of the electrode material. The supercapacitance application of the synthesized g-C$_3$N$_4$ and g-C$_3$N$_4$/cobaloxime composite materials has been examined by cyclic voltammetry (CV) and the galvanostatic charge−discharge (GCD) method.

The cyclic voltammetry (CV) studies of the prepared g-C$_3$N$_4$ and g-C$_3$N$_4$/cobaloxime nanocomposites have been analyzed at a scan rate 10−100 mV s$^{-1}$ in the potential range of 0.0−1.0 V (Figures 16 and S5). Figure 16a shows the CV of g-C$_3$N$_4$/C1 at different scan rates, and Figure 16b shows the

comparative CV of g-C$_3$N$_4$, cobaloxime (C1), and g-C$_3$N$_4$/C1 composites. The observed CV curves show quasi-rectangular peaks, indicating an ideal capacitive behavior. In addition, the CV curves of the prepared materials maintain the quasi-rectangular shape even at the higher scan rate, signifying the rapid charge−discharge property of the electrode materials.

The charge−discharge studies of g-C$_3$N$_4$ and g-C$_3$N$_4$/cobaloxime nanocomposites have been examined at various current densities from 0.5 to 5.0 A g$^{-1}$ in the same potential window range of 0.0−1.0 V. The charge−discharge curves of the prepared g-C$_3$N$_4$/cobaloxime composite electrode materials show higher discharging time when compared to pure g-C$_3$N$_4$ and cobaloxime C1. This longest time duration reveals the excellent capacitance behavior of the composite materials compared to the individual components. The nonlinear shapes of the charge−discharge curve reveal the EDLC (electrical double-layer capacitance) nature of the prepared electrode materials.

The charge−discharge curves of the composite g-C$_3$N$_4$/C1 at different current densities are presented in Figure 17a, and the remaining composites are provided in Figure S6. The comparative charge−discharge curve of g-C$_3$N$_4$, cobaloxime (C1), and g-C$_3$N$_4$/C1 composites is given in Figure 17b. The specific capacitance of the prepared electrode materials from the GCD studies is calculated using eq 1.

$$C_s = \frac{I \times \Delta t}{m \Delta V} \tag{1}$$

where $C_s$, $I$, $\Delta t$, $m$, and $\Delta V$ correspond to the specific capacitance (F g$^{-1}$), discharge current (mA), discharging time (s), mass of the prepared electrode material (g), and operating potential (V), respectively.

From eq 1, the calculated capacitance of the prepared g-C$_3$N$_4$, cobaloxime (C1), and g-C$_3$N$_4$/C1, g-C$_3$N$_4$/C2, g-C$_3$N$_4$/C3, and g-C$_3$N$_4$/C4 composite electrode materials at 0.5 A g$^{-1}$ are found to be 134, 125, 236, 199, 191, and 209 F g$^{-1}$, respectively. The data show that the specific capacitance decreases with an increase in current density, as expected for the supercapacitance behavior. The cobaloximes have a lower storage capacity than g-C$_3$N$_4$. However, the nanocomposites of g-C$_3$N$_4$/cobaloxime nanocomposites show higher specific capacitance than the g-C$_3$N$_4$ and cobaloxime complexes. Thus, the intercalation of metal complexes into the g-C$_3$N$_4$ nanomaterial offers good redox properties, thereby increasing
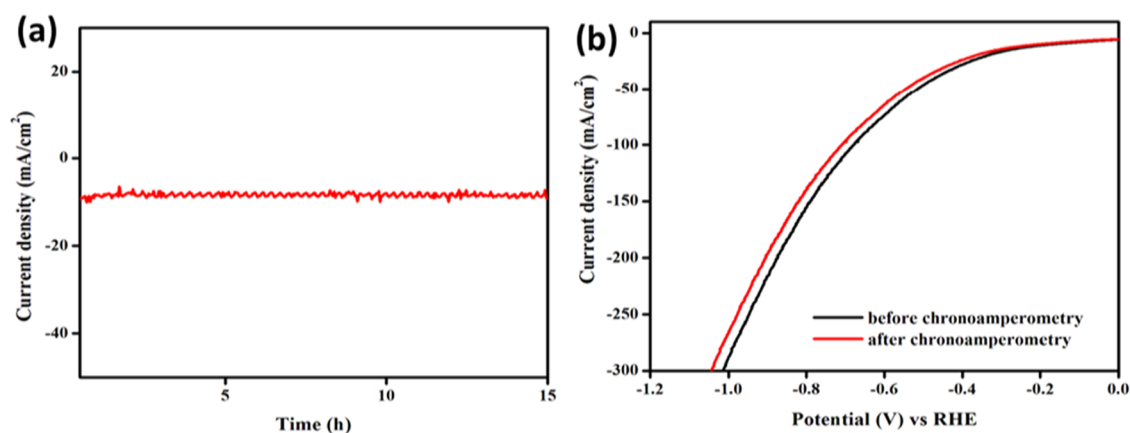


**Figure 12.** (a) Chronoamperometry curve of g-C$_3$N$_4$/C2 at a fixed potential of 173 mV vs RHE. (b) LSV curve before and after chronoamperometry.

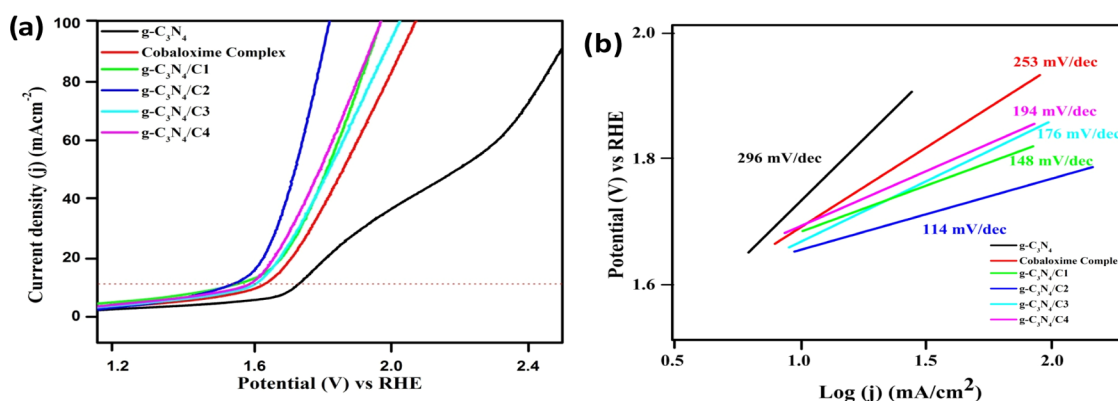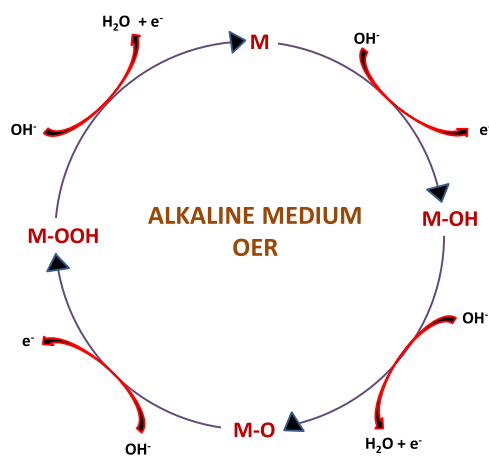**Figure 13.** (a) Linear sweep voltammograms of g-C$_3$N$_4$, cobaloxime complex C2, and g-C$_3$N$_4$/cobaloxime nanocomposites. (b) Tafel slope of g-C$_3$N$_4$, cobaloxime complex, and g-C$_3$N$_4$/cobaloxime nanocomposites for the OER in 0.5 M KOH.

**Scheme 3. Plausible Mechanism for the OER Reaction**



the charge transfer ability and also increasing the high accessibility of electroactive ions from electrolytes. Due to the high accessibility of electroactive ions, the charge–discharge capacity of the g-C$_3$N$_4$/cobaloxime nanocomposites shows a higher specific capacity than g-C$_3$N$_4$.

The specific capacitance of all four synthesized g-C$_3$N$_4$/cobaloxime nanocomposites has been studied in the current density range between 0.5 and 5.0 mA g$^{-1}$. Figure 18a shows the comparative specific capacitance of g-C$_3$N$_4$, cobaloxime complex **C1**, and all four synthesized g-C$_3$N$_4$/cobaloxime nanocomposites. It shows that g-C$_3$N$_4$/C1 is found to have the

highest specific capacitance at all current density ranges (0.5–5.0 mA) compared to the other composites. When the specific capacitance values of the composites studied in this work are compared with other g-C$_3$N$_4$ nanocomposites reported earlier (Table S4), the g-C$_3$N$_4$/cobaloxime nanocomposites show superior values than most of the other composites containing g-C$_3$N$_4$.[63−67]

Supercapacitor materials should have higher stability in order to improve their ability and durability in practical applications.[68] The stability of the electrode material g-C$_3$N$_4$/C1 nanocomposite has been studied using a charge−discharge cycle up to 7000 continuous cycle performance. Figure 18b shows the multiple charge−discharge graph of the g-C$_3$N$_4$/C1 electrode material. The studies show that the electrode material retained 82% stability at a 2.0 A g$^{-1}$ current density.

To gain further insights into the enhanced electrochemical activity of the catalyst, the electrochemical surface area (ESCA) of different catalysts has been calculated by using current in the nonfaradic region of the cyclic voltammograms at various scan rates from 10 to 100 mV s$^{-1}$. The double-layer capacitance ($C_{dl}$) is calculated from the slope values of the plot drawn between the current density and scan rate. Using the $C_{dl}$ value, ESCA can be calculated using the well-known formula ECSA = $C_{dl}/C_s$, where $C_s$ is the super capacitance of the electrode.[69] The ESCA calculated for all of the catalysts is provided in Figure 19. From the figure, it is seen that the g-C$_3$N$_4$ has a very less active surface of 0.74 mF cm$^{-2}$. The nanocomposites show a higher surface area than that of pure g-C$_3$N$_4$, which, in turn, show enhanced activity. Among the
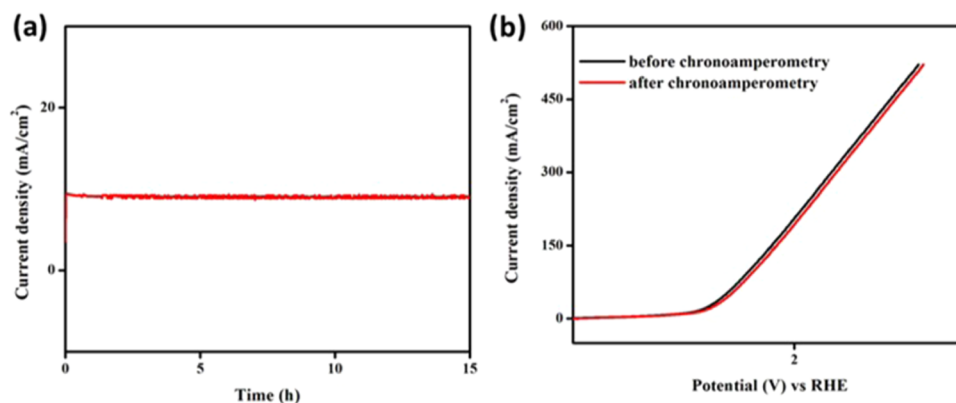


**Figure 14.** (a) Chronoamperometry of g-C$_3$N$_4$/C2 at a fixed potential of 303 mV vs RHE. (b) LSV curve before and after chronoamperometry.

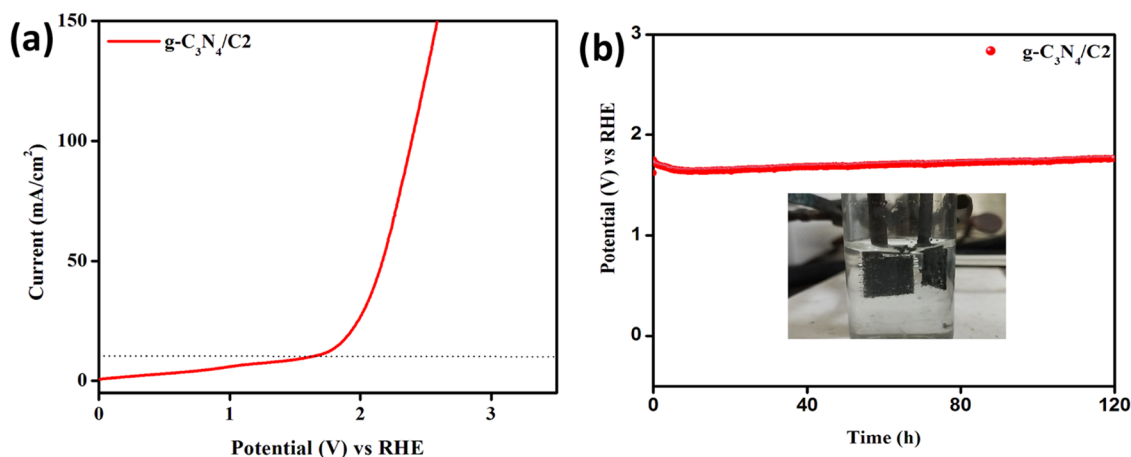**Figure 15.** (a) LSV of g-C$_3$N$_4$ in a two-electrode configuration at 100 mV s$^{-1}$ in 0.5 M KOH. (b) Overall water-splitting reaction in a two-electrode configuration at current densities of 10 mA cm$^{-2}$ in 0.5 M KOH (inset: the optical image showing hydrogen and oxygen production via bubble formation during water electrolysis).
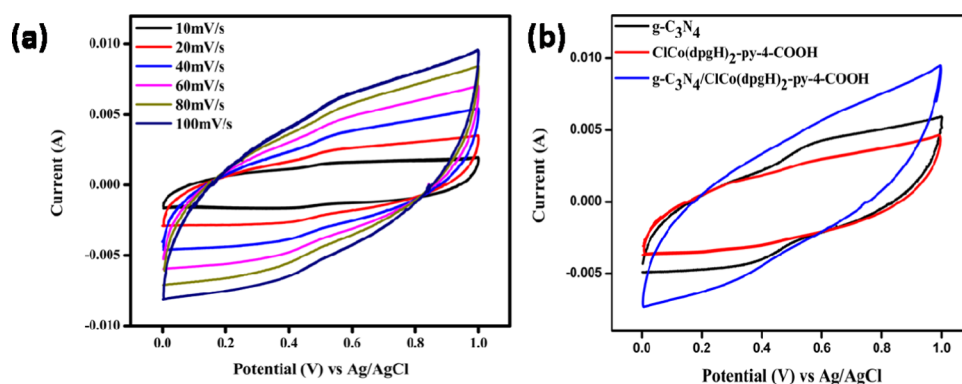


**Figure 16.** (a) Cyclic voltammograms of g-C$_3$N$_4$/C1 at different scan rates (10−100 mV s$^{-1}$). (b) Comparison of cyclic voltammograms of g-C$_3$N$_4$, cobaloxime complex (C1), and g-C$_3$N$_4$/C1 at 100 mV s$^{-1}$.
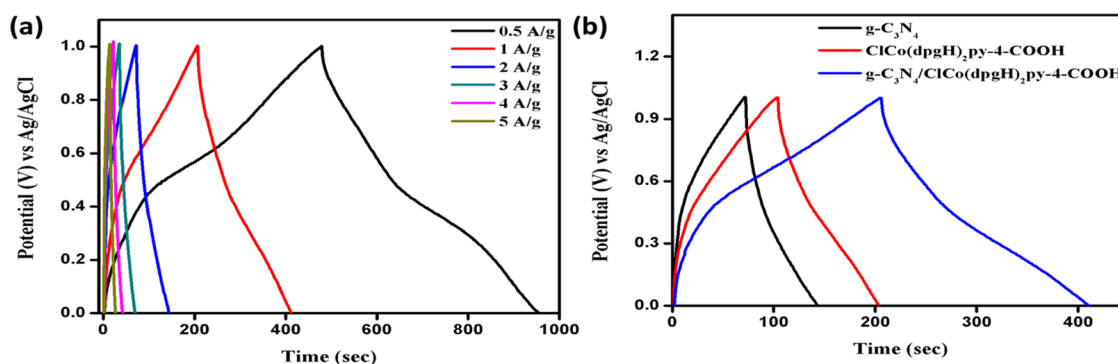


**Figure 17.** (a) g-C$_3$N$_4$/C1 charge−discharge curve of g-C$_3$N$_4$/C1 at different current densities (0.5−5.0 A g$^{-1}$). (b) Comparative charge−discharge curve of g-C$_3$N$_4$, cobaloxime complex C1, and g-C$_3$N$_4$/C1 at 1.0 A g$^{-1}$.

nanocomposites, g-C$_3$N$_4$/C1 has a higher surface area of 2.10 mF cm$^{-2}$ than the other three composites. It has better super capacitance ability among the four composites and also shows good HER and OER activity.[70]

The composite g-C$_3$N$_4$/C2 has a surface area of 1.90 mF cm$^{-2}$, which is only 0.2 mF cm$^{-2}$ lower than that of g-C$_3$N$_4$/C1 and shows better HER and OER activity. The g-C$_3$N$_4$/C3 and g-C$_3$N$_4$/C4 composites have a surface area of 1.72 and 1.17 mF cm$^{-2}$, respectively. The studies indicate that the composites g-C$_3$N$_4$/C1 and g-C$_3$N$_4$/C2 have more accessible active sites than the other composites, g-C$_3$N$_4$/C1 bears good

supercapacitance, and g-C$_3$N$_4$/C2 possesses better water-splitting ability.

## 4. CONCLUSIONS

In summary, four cobaloximes, g-C$_3$N$_4$, and g-C$_3$N$_4$/cobaloxime (C1, C2, C3, C4) nanocomposites have been synthesized, and the synthesized nanocomposites have been characterized by Fourier transform infrared (FTIR) spectroscopy, UV-DRS, XRD, XPS, SEM, PSA, TEM, HRTEM, BET, and EDAX analyses. The synthesized composites have been tested toward their HER, OER, and supercapacitance ability, and all of them

**Figure 18.** (a) Comparative Specific capacitance of g-$C_3N_4$, cobaloxime complex C1,and g-$C_3N_4$/C1, g-$C_3N_4$/C2, g-$C_3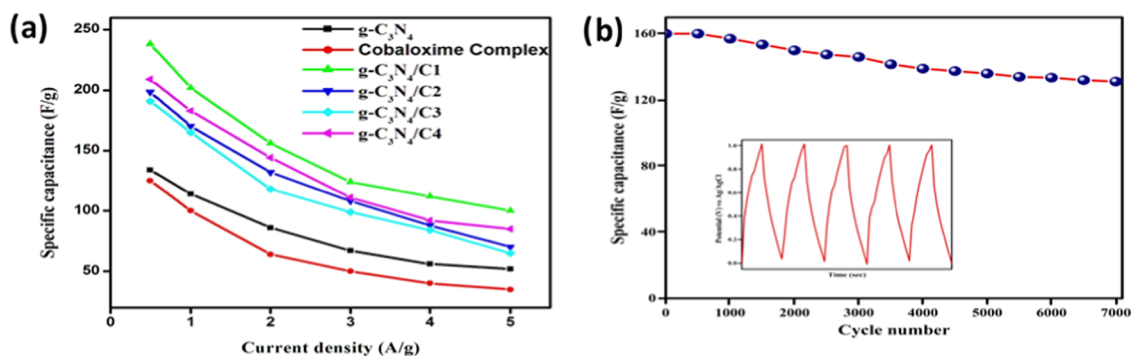N_4$/C3, and g-$C_3N_4$/C4. (b) Cycling stability of g-$C_3N_4$/C1 at a 2.0 A g$^{-1}$ current density up to 7000 cycles.
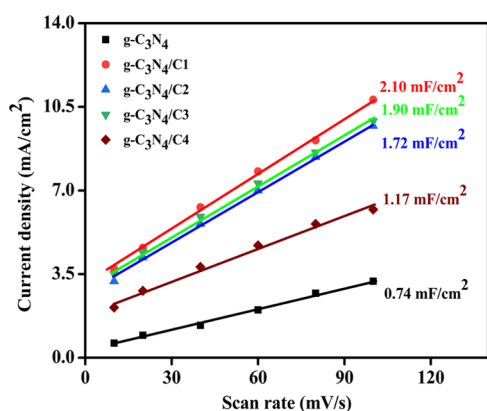


**Figure 19.** ECSA analysis of g-$C_3N_4$, g-$C_3N_4$/C1, g-$C_3N_4$/C2, g-$C_3N_4$/C3, and g-$C_3N_4$/C4.

behave as multifunctional catalysts, showing good electrochemical energy conversion and storage capability. Among the synthesized g-$C_3N_4$/cobaloxime nanocomposites, composite g-$C_3N_4$/C2 functions as a good bifunctional catalyst toward HER and OER as it affords excellent HER activity with a lower overpotential of 173 mV at −10 mA cm$^{-2}$ and OER activity with a lower overpotential of 303 mV. The overall electrocatalytic water-splitting studies indicate that the hydrogen and oxygen evolution process is undisturbed for at least 120 h. The storage capacity studies of the synthesized g-$C_3N_4$/cobaloxime composites reveal that among the prepared nanocomposites, the composite g-$C_3N_4$/C1 possesses good storage capacity with a specific capacitance of 236 F g$^{-1}$ with an 82% capacity retention up to 7000 cycles. The studies also indicate that the g-$C_3N_4$/cobaloxime nanocomposites behave as better electrochemical storage devices compared to other catalysts with g-$C_3N_4$ as the catalyst support. The improved catalytic activity of g-$C_3N_4$ is due to the more active sites provided by g-$C_3N_4$, the introduction of cobalt metal into the g-$C_3N_4$ matrix that improves the redox property of the composites, and the presence of an electron-withdrawing carboxylic acid group.

## ■ ASSOCIATED CONTENT

### Ⓢ Supporting Information

The Supporting Information is available free of charge at https://pubs.acs.org/doi/10.1021/acsomega.3c04347.

Tauc plot (Figure S1); XRD images of (a) cobaloxime, g-$C_3N_4$, g-$C_3N_4$/C3, and g-$C_3N_4$/C4 and (b) zoom XRD image of g-$C_3N_4$, g-$C_3N_4$/C3, and g-$C_3N_4$/C4 (Figure S2); EDAX spectrum of (a) g-$C_3N_4$ and (b)

cobaloxime (Figure S3); SEM of catalyst g-$C_3N_4$/C2 after the stability test (Figure S4); CV curves of (a) g-$C_3N_4$/C2, (b) g-$C_3N_4$/C3, and (c) g-$C_3N_4$/C4 (Figure S5); CD curves of (a) g-$C_3N_4$/C2, (b) g-$C_3N_4$/C3, and (c) g-$C_3N_4$/C4 (Figure S4); band gap of g-$C_3N_4$ and g-$C_3N_4$/nanocomposites (Table S1); EDAX analysis of g-$C_3N_4$, cobaloxime, and g-$C_3N_4$/cobaloxime (C1) (Table S2); comparative OER and HER Tafel slopes (Table S3); and comparative specific capacitance values (Table S4) (PDF)

## ■ AUTHOR INFORMATION

### Corresponding Author

**Vijendran Vijaikanth** − *Department of Applied Chemistry, Karunya Institute of Technology and Sciences, Coimbatore 641114 Tamilnadu, India;* ⓞ orcid.org/0000-0002-8812-9751; Email: vvijaikanth@gmail.com

### Author

**Subramanian Sowmya** − *Department of Applied Chemistry, Karunya Institute of Technology and Sciences, Coimbatore 641114 Tamilnadu, India*

Complete contact information is available at:
https://pubs.acs.org/10.1021/acsomega.3c04347

### Notes

The authors declare no competing financial interest.

## ■ REFERENCES

(1) Song, L.; Sun, S.; Zhang, S.; Wei, J. Hydrogen Production and Mechanism from Water Splitting by Metal-Free Organic Polymers PVDF/PVDF-HFP under Drive by Vibrational Energy. *Fuel* **2022**, *324*, No. 124572.

(2) Van Phuc, T.; Jana, J.; Ravi, N.; Kang, S. G.; Chung, J. S.; Choi, W. M.; Hur, S. H. Highly Active Ni/Co-Metal Organic Framework Bifunctional Electrocatalyst for Water Splitting Reaction. *Int. J. Hydrogen Energy* **2022**, *47* (54), 22787−22795.

(3) Armaroli, N.; Balzani, V. The Future of Energy Supply: Challenges and Opportunities. *Angew. Chem., Int. Ed.* **2007**, *46* (1−2), 52−66.

(4) Sun, Z.; Xin, F.; Cao, C.; Zhao, C.; Shen, C.; Han, W. Q. Hollow Silica−Copper−Carbon Anodes Using Copper Metal−Organic Frameworks as Skeletons. *Nanoscale* **2015**, *7* (48), 20426−20434.

(5) Wei, D.; Xu, F.; Xu, J.; Fang, J.; Koh, S. W.; Li, K.; Sun, Z. Three-Dimensional Porous $SnO_2$@NC Framework for Excellent Energy Conversion and Storage. *Ceram. Int.* **2020**, *46* (2), 1396−1402.

(6) Du, P.; Eisenberg, R. Catalysts Made of Earth-Abundant Elements (Co, Ni, Fe) for Water Splitting: Recent Progress and Future Challenges. *Energy Environ. Sci.* **2012**, *5* (3), 6012−6021.

(7) Benson, E. E.; Kubiak, C. P.; Sathrum, A. J.; Smieja, J. M. Electrocatalytic and Homogeneous Approaches to Conversion of $CO_2$ to Liquid Fuels. *Chem. Soc. Rev.* **2009**, *38* (1), 89−99.

(8) Thoi, V. S.; Sun, Y.; Long, J. R.; Chang, C. J. Complexes of Earth-Abundant Metals for Catalytic Electrochemical Hydrogen Generation under Aqueous Conditions. *Chem. Soc. Rev.* **2013**, *42* (6), 2388−2400.

(9) Ding, Y.; Miao, B. Q.; Li, S. N.; Jiang, Y. C.; Liu, Y. Y.; Yao, H. C.; Chen, Y. Benzylamine Oxidation Boosted Electrochemical Water-Splitting: Hydrogen and Benzonitrile Co-Production at Ultra-Thin Ni2P Nanomeshes Grown on Nickel Foam. *Appl. Catal., B* **2020**, *268*, No. 118393.

(10) Nie, Y.; Li, L.; Wei, Z. Recent Advancements in Pt and Pt-Free Catalysts for Oxygen Reduction Reaction. *Chem. Soc. Rev.* **2015**, *44* (8), 2168−2201.

(11) Da Silva, G. C.; Fernandes, M. R.; Ticianelli, E. A. Activity and Stability of Pt/$IrO_2$ Bifunctional Materials as Catalysts for the Oxygen Evolution/Reduction Reactions. *ACS Catal.* **2018**, *8* (3), 2081−2092.

(12) Jiang, J.; Wang, C.; Zhang, J.; Wang, W.; Zhou, X.; Pan, B.; Tang, K.; Zuo, J.; Yang, Q. Synthesis of $FeP_2$/C Nanohybrids and Their Performance for Hydrogen Evolution Reaction. *J. Mater. Chem. A* **2015**, *3* (2), 499−503.

(13) Wang, D. Y.; Gong, M.; Chou, H. L.; Pan, C. J.; Chen, H. A.; Wu, Y.; Lin, M. C.; Guan, M.; Yang, J.; Chen, C. W.; Wang, Y. L.; Hwang, B. J.; Chen, C. C.; Dai, H. Highly Active and Stable Hybrid Catalyst of Cobalt-Doped $FeS_2$ Nanosheets-Carbon Nanotubes for Hydrogen Evolution Reaction. *J. Am. Chem. Soc.* **2015**, *137* (4), 1587−1592.

(14) Li, H.; Qian, X.; Zhu, C.; Jiang, X.; Shao, L.; Hou, L. Template Synthesis of $CoSe_2$/$Co_3Se_4$ Nanotubes: Tuning of Their Crystal Structures for Photovoltaics and Hydrogen Evolution in Alkaline Medium. *J. Mater. Chem. A* **2017**, *5* (9), 4513−4526.

(15) Liu, Z.; Yu, X.; Xue, H.; Feng, L. A Nitrogen-Doped CoP Nanoarray over 3D Porous Co Foam as an Efficient Bifunctional Electrocatalyst for Overall Water Splitting. *J. Mater. Chem. A* **2019**, *7* (21), 13242−13248.

(16) Sun, P. P.; Zhang, Y. H.; Mu, J.; Tian, B.; Shi, F. N. Structure and Electrochemical Performance of a GeMo Bimetal Complex as Anodes for Lithium Ion Batteries and Supercapacitors. *Inorg. Chem. Commun.* **2021**, *125*, No. 108436.

(17) Sharma, P.; Bhatti, T. S. A Review on Electrochemical Double-Layer Capacitors. *Energy Convers. Manag.* **2010**, *51* (12), 2901−2912.

(18) Wang, Y.; Xia, Y. Recent Progress in Supercapacitors: From Materials Design to System Construction. *Adv. Mater.* **2013**, *25* (37), 5336−5342.

(19) Zhang, X.; Yang, P.; Jiang, S. P. Ni Diffusion in Vertical Growth of $MoS_2$ Nanosheets on Carbon Nanotubes towards Highly Efficient Hydrogen Evolution. *Carbon* **2021**, *175*, 176−186.

(20) Parnell, C. M.; Watanabe, F.; Nasini, U. B.; Berry, B. C.; Mitchell, T.; Shaikh, A. U.; Ghosh, A. Electrochemical Sensing of Hydrogen Peroxide Using a Cobalt(III) Complex Supported on Carbonaceous Nanomaterials. *J. Electroanal. Chem.* **2015**, *740*, 37−44.

(21) Zhang, H.; Xu, B.; Zhang, X.; Yang, P. Raspberry-like TiO2 Hollow Spheres Consisting of Small Nanocrystals towards Efficient NO Removal. *Environ. Sci. Nano* **2022**, *9* (9), 3397−3406.

(22) Zhang, X.; Matras-Postolek, K.; Yang, P. Heterojunction Nanoarchitectonics of WOx/Au-g-$C_3N_4$ with Efficient Photogenerated Carrier Separation and Transfer toward Improved NO and Benzene Conversion. *Mater. Today Adv.* **2023**, *17*, No. 100355.

(23) Zhang, X.; Ran Zhang, X.; Yang, P.; Chen, H.-S.; Ping Jiang, S. Black Magnetic Cu-g-$C_3N_4$ Nanosheets towards Efficient Photocatalytic $H_2$ Generation and $CO_2$/Benzene Conversion. *Chem. Eng. J.* **2022**, *450*, No. 138030.

(24) Zhang, X.; Matras-Postolek, K.; Yang, P.; Ping Jiang, S. Z-Scheme WOx/Cu-g-$C_3N_4$ Heterojunction Nanoarchitectonics with Promoted Charge Separation and Transfer towards Efficient Full Solar-Spectrum Photocatalysis. *J. Colloid Interface Sci.* **2023**, *636*, 646−656.

(25) Zhang, X.; Zhang, X.; Yang, P.; Jiang, S. P. Layered Graphitic Carbon Nitride: Nano-Heterostructures, Photo/Electro-Chemical Performance and Trends. *J. Nanostruct. Chem.* **2022**, *12* (5), 669−691.

(26) Zhang, X.; Yang, P.; Jiang, S. P. Ni Clusters-Derived 2D/2D Layered WOx($MoS_2$)/Ni-g-$C_3N_4$ Step-Scheme Heterojunctions with Enhanced Photo- and Electro-Catalytic Performance. *J. Power Sources* **2021**, *510*, No. 230420.

(27) Song, T.; Zhang, X.; Yang, P. Interface Engineering of $W_2C$/$W_2N$ Co-Catalyst on g-C3N4 Nanosheets for Boosted $H_2$ Evolution and 4-Nitrophenol Removal. *Environ. Sci. Nano* **2022**, *9* (5), 1888−1899.

(28) Ma, T. Y.; Ran, J.; Dai, S.; Jaroniec, M.; Qiao, S. Z. Phosphorus-Doped Graphitic Carbon Nitrides Grown In Situ on Carbon-Fiber Paper: Flexible and Reversible Oxygen Electrodes. *Angew. Chem., Int. Ed.* **2015**, *54* (15), 4646−4650.

(29) Tian, J.; Liu, Q.; Asiri, A. M.; Alamry, K. A.; Sun, X. Ultrathin Graphitic $C_3N_4$ Nanosheets/Graphene Composites: Efficient Organic Electrocatalyst for Oxygen Evolution Reaction. *ChemSusChem* **2014**, *7* (8), 2125−2130.

(30) Cao, S. W.; Liu, X. F.; Yuan, Y. P.; Zhang, Z. Y.; Fang, J.; Loo, S. C. J.; Barber, J.; Sum, T. C.; Xue, C. Artificial Photosynthetic Hydrogen Evolution over G-$C_3N_4$ Nanosheets Coupled with Cobaloxime. *Phys. Chem. Chem. Phys.* **2013**, *15* (42), 18363−18366.

(31) Rashid, J.; Parveen, N.; Haq, T. ul; Iqbal, A.; Talib, S. H.; Awan, S. U.; Hussain, N.; Zaheer, M. G-$C_3N_4$/$CeO_2$/$Fe_3O_4$ Ternary Composite as an Efficient Bifunctional Catalyst for Overall Water Splitting. *ChemCatChem* **2018**, *10* (24), 5587−5592.

(32) Zheng, Y.; Jiao, Y.; Zhu, Y.; Cai, Q.; Vasileff, A.; Li, L. H.; Han, Y.; Chen, Y.; Qiao, S. Z. Molecule-Level g-$C_3N_4$ Coordinated Transition Metals as a New Class of Electrocatalysts for Oxygen Electrode Reactions. *J. Am. Chem. Soc.* **2017**, *139* (9), 3336−3339.

(33) Zhong, H. X.; Zhang, Q.; Wang, J.; Zhang, X. B.; Wei, X. L.; Wu, Z. J.; Li, K.; Meng, F. L.; Bao, D.; Yan, J. M. Engineering Ultrathin $C_3N_4$ Quantum Dots on Graphene as a Metal-Free Water Reduction Electrocatalyst. *ACS Catal.* **2018**, *8* (5), 3965−3970.

(34) Reuillard, B.; Warnan, J.; Leung, J. J.; Wakerley, D. W.; Reisner, E. A Poly(Cobaloxime)/Carbon Nanotube Electrode: Freestanding Buckypaper with Polymer-Enhanced H2-Evolution Performance. *Angew. Chem.* **2016**, *128* (12), 4020−4025.

(35) Wadsworth, B. L.; Beiler, A. M.; Khusnutdinova, D.; Jacob, S. I.; Moore, G. F. Electrocatalytic and Optical Properties of Cobaloxime Catalysts Immobilized at a Surface-Grafted Polymer Interface. *ACS Catal.* **2016**, *6* (12), 8048−8057.

(36) Özçeşmeci, İ.; Demir, A.; Akyüz, D.; Koca, A.; Gül, A. Electrocatalytic Hydrogen Evolution Reaction with a Supramolecular Cobalt(II)Phthalocyanine Carrying Four Cobaloxime Moieties. *Inorg. Chim. Acta* **2017**, *466*, 591−598.

(37) Shajaripour Jaberi, S. Y.; Ghaffarinejad, A. A Graphite Sheet Modified with Reduced Graphene Oxide-Hyper-Branched Gold Nanostructure as a Highly Efficient Electrocatalyst for Hydrogen Evolution Reaction. *Int. J. Hydrogen Energy* **2019**, *44* (57), 29922−29932.

(38) Xia, W.; Mahmood, A.; Zou, R.; Xu, Q. Metal−Organic Frameworks and Their Derived Nanostructures for Electrochemical Energy Storage and Conversion. *Energy Environ. Sci.* **2015**, *8* (7), 1837−1866.

(39) Ke, F. S.; Solomon, B. C.; Ma, S. G.; Zhou, X. D. Metal−Carbon Nanocomposites as the Oxygen Electrode for Rechargeable Lithium−Air Batteries. *Electrochim. Acta* **2012**, *85*, 444−449.

(40) Sowmya, S.; Vijaikanth, V. Electrochemistry and Electrocatalytic Activity of Cobaloxime Complexes. *ChemistrySelect* **2022**, 7 (10), No. e202104044, DOI: 10.1002/slct.202104044.

(41) Cai, M.; Zhang, F.; Zhang, C.; Lu, C.; He, Y.; Qu, Y.; Tian, H.; Feng, X.; Zhuang, X. Cobaloxime Anchored MoS2 Nanosheets as Electrocatalysts for the Hydrogen Evolution Reaction. *J. Mater. Chem. A* **2018**, 6 (1), 138−144.

(42) Sideri, I. K.; Charalambidis, G.; Coutsolelos, A. G.; Arenal, R.; Tagmatarchis, N. Pyridine vs. Imidazole Axial Ligation on Cobaloxime Grafted Graphene: Hydrogen Evolution Reaction Insights. *Nanomaterials* **2022**, 12 (17), No. 3077.

(43) Roy, S.; Huang, Z.; Bhunia, A.; Castner, A.; Gupta, A. K.; Zou, X.; Ott, S. Electrocatalytic Hydrogen Evolution from a Cobaloxime-Based Metal-Organic Framework Thin Film. *J. Am. Chem. Soc.* **2019**, 141 (40), 15942−15950.

(44) Gottschling, K.; Savasci, G.; Vignolo-González, H.; Schmidt, S.; Mauker, P.; Banerjee, T.; Rovó, P.; Ochsenfeld, C.; Lotsch, B. V. Rational Design of Covalent Cobaloxime-Covalent Organic Framework Hybrids for Enhanced Photocatalytic Hydrogen Evolution. *J. Am. Chem. Soc.* **2020**, 142 (28), 12146−12156.

(45) Sowmya, S.; Sridhar, L.; Vijaikanth, V. Preparation and Characterization of Glassy Carbon Electrode Modified with Cobaloximes Containing Diphenylglyoxime. *Mater. Today Proc.* **2021**, 47, 784−789.

(46) Sowmya, S.; Paul, P. M.; Boopalan, S.; Abiram, A.; Michaud, F.; Vijaikanth, V. Synthesis, Crystal Structure and Electrocatalytic Hydrogen Evolution Reaction Studies of Cobaloximes with Diphenylglyoxime and Carboxylic Acid Functionalized Neutral Bases. *Polyhedron* **2023**, 238, No. 116394.

(47) Dong, F.; Wu, L.; Sun, Y.; Fu, M.; Wu, Z.; Lee, S. C. Efficient Synthesis of Polymeric G-C3N4 Layered Materials as Novel Efficient Visible Light Driven Photocatalysts. *J. Mater. Chem.* **2011**, 21 (39), 15171−15174.

(48) Bhat, S. A.; Rashid, N.; Rather, M. A.; Pandit, S. A.; Ingole, P. P.; Bhat, M. A. Vitamin B12 Functionalized N-Doped Graphene: A Promising Electro-Catalyst for Hydrogen Evolution and Electro-Oxidative Sensing of H2O2. *Electrochim. Acta* **2020**, 337, No. 135730.

(49) Jiang, D.; Chen, L.; Xie, J.; Chen, M. Ag2S/g-C3N4 Composite Photocatalysts for Efficient Pt-Free Hydrogen Production. The Co-Catalyst Function of Ag/Ag2S Formed by Simultaneous Photodeposition. *Dalton Trans.* **2014**, 43 (12), 4878−4885.

(50) Boopalan, S.; Antony, A.; Loyid, N. S.; Vijaikanth, V.; Murugan, S. Synthesis, Characterization, X-Ray Crystal Structures and Antibacterial Properties of Cobaloximes with Aniline Based Ligands Containing Acid Functionality. In *Inorganic and Nano-Metal Chemistry*; Taylor & Francis, 2022.

(51) Zhang, H.; Park, S. O.; Seo, J. H.; Joo, S. H.; Huang, M.; Wang, C.; Wang, M.; Kwak, S. K.; Ruoff, R. S. Topochemical Intercalation of Graphitic Carbon Nitride with Alkali Metals in Ethylenediamine. *J. Phys. Chem. C* **2021**, 125 (18), 9947−9955.

(52) Gaya, U. I.; Sani, K. I.; Hamisu, A. Synthesis of Visible Light Response S-SnO2 Catalyst for Optimized Photodegradation of Bromophenol Blue. *J. Phys. Chem. Funct. Mater.* **2021**, 4 (2), 22−33.

(53) Song, X. W.; Wen, H. M.; Ma, C. B.; Cui, H. H.; Chen, H.; Chen, C. N. Efficient Photocatalytic Hydrogen Evolution with End-Group-Functionalized Cobaloxime Catalysts in Combination with Graphite-like C3N4. *RSC Adv.* **2014**, 4 (36), 18853−18861.

(54) Feng, D.; Cheng, Y.; He, J.; Zheng, L.; Shao, D.; Wang, W.; Wang, W.; Lu, F.; Dong, H.; Liu, H.; Zheng, R.; Liu, H. Enhanced Photocatalytic Activities of G-C3N4 with Large Specific Surface Area via a Facile One-Step Synthesis Process. *Carbon* **2017**, 125, 454−463.

(55) Rabani, I.; Zafar, R.; Subalakshmi, K.; Kim, H. S.; Bathula, C.; Seo, Y. S. A Facile Mechanochemical Preparation of Co3O4@g-C3N4 for Application in Supercapacitors and Degradation of Pollutants in Water. *J. Hazard. Mater.* **2021**, 407, No. 124360.

(56) Mousavi, M.; Hamzehloo, M.; Ghasemi, J. B. Deposited CuBi2O4 and Bi3ClO4 Nanoparticles on G-C3N4 Nanosheet: A Promising Visible Light-Induced Photocatalyst toward the Removal of Tetracycline Hydrochloride and Rhodamine B. *J. Mater. Sci.* **2020**, 55 (18), 7775−7791.

(57) Riyajuddin, S.; Tarik Aziz, S. K.; Kumar, S.; Nessim, G. D.; Ghosh, K. 3D-Graphene Decorated with g-C3N4/Cu3P Composite: A Noble Metal-Free Bifunctional Electrocatalyst for Overall Water Splitting. *ChemCatChem* **2020**, 12 (5), 1394−1402.

(58) Zang, M.; Xu, N.; Cao, G.; Chen, Z.; Cui, J.; Gan, L.; Dai, H.; Yang, X.; Wang, P. Cobalt Molybdenum Oxide Derived High-Performance Electrocatalyst for the Hydrogen Evolution Reaction. *ACS Catal.* **2018**, 8, 5062.

(59) Mei, T.; Gao, M.; Liu, D.; Wang, Y.; Huang, Y. Enhanced Electrocatalytic Activity of Carbon Cloth by Synergetic Effect of Plasma and Acid Treatment. *Plasma Sci. Technol.* **2021**, 23 (2), No. 025504, DOI: 10.1088/2058-6272/abd8b4.

(60) Zhang, G.; Wang, P.; Lu, W. T.; Wang, C. Y.; Li, Y. K.; Ding, C.; Gu, J.; Zheng, X. S.; Cao, F. F. Co Nanoparticles/Co, N, S Tri-Doped Graphene Templated from In-Situ-Formed Co, S Co-Doped g-C3N4 as an Active Bifunctional Electrocatalyst for Overall Water Splitting. *ACS Appl. Mater. Interfaces* **2017**, 9 (34), 28566−28576.

(61) Zhang, B.; Li, J.; Song, Q.; Lv, S.; Shi, Y.; Liu, H. G-C3N4-Modulated Bifunctional SnO2@g-C3N4@SnS2 Hollow Nanospheres for Efficient Electrochemical Overall Water Splitting. *Appl. Surf. Sci.* **2022**, 589, No. 153016.

(62) Arif, M.; Yasin, G.; Shakeel, M.; Fang, X.; Gao, R.; Ji, S.; Yan, D. Coupling of Bifunctional CoMn-Layered Double Hydroxide@ Graphitic C3N4 Nanohybrids towards Efficient Photoelectrochemical Overall Water Splitting. *Chem. − Asian J.* **2018**, 13 (8), 1045−1052.

(63) Xu, L.; Xia, J.; Xu, H.; Yin, S.; Wang, K.; Huang, L.; Wang, L.; Li, H. Reactable Ionic Liquid Assisted Solvothermal Synthesis of Graphite-like C3N4 Hybridized α-Fe2O3 Hollow Microspheres with Enhanced Supercapacitive Performance. *J. Power Sources* **2014**, 245, 866−874.

(64) Tahir, M.; Cao, C.; Butt, F. K.; Idrees, F.; Mahmood, N.; Ali, Z.; Aslam, I.; Tanveer, M.; Rizwan, M.; Mahmood, T. Tubular Graphitic-C3N4: A Prospective Material for Energy Storage and Green Photocatalysis. *J. Mater. Chem. A* **2013**, 1 (44), 13949−13955.

(65) Kavil, J.; Anjana, P. M.; Periyat, P.; Rakhi, R. B. One-Pot Synthesis of g-C3N4/MnO2 and g-C3N4/SnO2 Hybrid Nanocomposites for Supercapacitor Applications. *Sustainable Energy Fuels* **2018**, 2 (10), 2244−2251.

(66) Gonçalves, R.; Lima, T. M.; Paixão, M. W.; Pereira, E. C. Pristine Carbon Nitride as Active Material for High-Performance Metal-Free Supercapacitors: Simple, Easy and Cheap. *RSC Adv.* **2018**, 8 (61), 35327−35336.

(67) Lu, C.; Chen, X. Porous G-C3N4 Covered MOF-Derived Nanocarbon Materials for High-Performance Supercapacitors. *RSC Adv.* **2019**, 9 (67), 39076−39081.

(68) Goswami, L.; Kushwaha, A.; Goswami, S.; Sharma, Y. C.; Kim, T. Y.; Tripathi, K. M.Nanocarbon-Based-ZnO Nanocomposites for Supercapacitor Application. In *Nanostructured Zinc Oxide: Synthesis, Properties and Applications*; Elsevier, 2021; pp 553−573.

(69) Krishna Sadhanala, H.; Gupta, A.; Gedanken, A. Ultra-Low Palladium Engineered Nickel Sulfide Heterostructure Supported on 3D Nickel Foam as a Highly Efficient and Stable Electrocatalyst for Water Oxidation. *J. Electroanal. Chem.* **2022**, 926, No. 116931.

(70) Santos, H. L. S.; Corradini, P. G.; Medina, M.; Dias, J. A.; Mascaro, L. H. NiMo-NiCu Inexpensive Composite with High Activity for Hydrogen Evolution Reaction. *ACS Appl. Mater. Interfaces* **2020**, 12 (15), 17492−17501.